The Variety of Spontaneously Generated Tropical Precipitation Patterns found in APE Results

Kensuke NAKAJIMA

Faculty of Sciences, Kyushu University, Fukuoka, Japan

and

Yukiko YAMADA

Graduate School of Science, Hokkaido University, Sapporo, Japan

and

Yoshiyuki O. TAKAHASHI

Center for Planetary Sciences, Kobe, Japan
Kobe University, Kobe, Japan

and

Masaki ISHIWATARI

Faculty of Science, Hokkaido University, Sapporo, Japan

and

Wataru OHFUCHI

Earth Simulator Center, Japan Agency of Marine Science and Technology, Yokohama, Japan

and

Yoshi-Yuki HAYASHI

Center for Planetary Sciences, Kobe, Japan
Kobe University, Kobe, Japan

August 17, 2012

Corresponding author: Kensuke Nakajima, Faculty of Sciences, Kyushu University, 6-10-1, Hakozaki, Fukuoka, Fukuoka 812-8581, Japan.
E-mail: kensuke@geo.kyushu-u.ac.jp

Abstract

We examine the results of the Aqua-Planet Experiment Project (APE) focusing mainly on the structure of equatorial precipitation in the subset of participating models for which the details of model variables are available. In spite of the unified set-up of the APE, the Hovmëllor plots of precipitation in the models exhibit wide range of diversity, presumably resulting from the diversity among implementations of various physical processes. Nevertheless, the wavenumber-frequency spectra of precipitation exhibit certain degree of similarity; the power spectra can be divided into Kelvin, westward inertio gravity, and "advective" components. The intensity of each of these three components varies significantly among different models. The composite spatial structures corresponding to the above three components are produced by performing regression analysis with space-time filtered data. The composite horizontal structures of the Kelvin and westward inertio gravity components are similar among the models and resemble to those expected from the corresponding equatorial shallow water wave modes. These resemblances degrade at the altitude levels where the value of phase velocity is near the zonal mean zonal wind speed. The horizontal structures of the "advective" component diverge significantly among models. The composite vertical structures are strongly model dependent for all of the three components. The comparison among vertical and horizontal structures of con-

vective and stratiform heating of the composite disturbances indicates that the diversity of vertical structures originates from the difference in physical processes, especially, the implementation of cumulus parameterization.

1. Introduction

Convective activity in the earth's tropical atmosphere is recognized to exhibit a hierarchical structure including individual cumulonimbi, mesoscale features, cloud clusters (Houze and Betts 1981), various kinds of synoptic scale disturbances such as convectively coupled equatorial waves (Kiladis et al. 2009), intraseasonal variability (ISV) (Madden and Julian 1972), and climatological features like the intertropical convergence zone (ITCZ) or the convection centers. Each of the classes in the hierarchy has unique importance in the role, for example, in the maintenance of the climate system (Sherwood et al. 2010), in predictability issues of numerical weather prediction, and in severe meteorological phenomena central to the disaster prevention. Reproduction and understanding of the hierarchy of convective activity is thus one of the most important theme of tropical meteorology.

In our efforts to capture the hierarchical structure, there remains a large degree of difficulty. The most obvious difficulty is its extremely wide range of spatial and temporal scales; there is four orders of magnitude difference from the smallest member, individual cumulonimbi having 1–10 km scale, to the largest member, ISV and ITCZ having a global scale. If we wish to simulate whole of the hierarchical structure explicitly, we have to run a global cumulus resolving model; its execution requires huge computational resources (Tao and Moncrieff 2009). Up to present, only a very limited number of such explicit calculations have been accomplished (Satoh et al. 2008). Other than such explicit simulations, any kinds of global models are, more or less, compromised to incorporate the effects of the smaller classes of the hierarchy, i.e., cumulonimbi and mesoscale systems. The most common way of compromise has been to employ cumulus parameterization, although there are a few exceptional attempts to avoid cumulus parameterization by using "distorted" dynamical equations (Kuang et al. 2005).

Although it is true that computational resources are rapidly developing, a certain level of cumulus parameterization is considered to remain in global models at least for long term simulations like those for the projection of possible global warming. And hence, the knowledge on the performance of numerical models employing cumulus parameterizations in the reproduction of the tropical convection hierarchy remains important in some unforeseeable period in the future. At present, there are not small number of cumulus parameterization used in operational or community atmospheric models including adjustment type schemes (Manabe et al. 1965), mass flux type schemes (Tiedtke 1989), and schemes employing ensemble of cumulus (Arakawa and Schubert 1974). In spite that a cumulus parameterization scheme is highly tuned to reproduce the behavior of the real atmosphere when used in an atmospheric model, it has been known that the properties of tropical atmospheric convection represented in numerical models exhibit wide variety among models, and it is still agreed that no single specific parameterization scheme can be nominated as the one that is the most suitable for reproducing the reality. We have to examine how and why various models behave differently by comparing the results with such models in a common setup as an inter comparison project such as Atmospheric Model Intercomparison Project (AMIP) or Coupled Model Intercomparison Project (CMIP).

The Aqua-Planet Experiment Project (APE) is an attempt to compare the behavior of modern sophisticated numerical models used for numerical weather prediction or climate simulation in the simplest set-up of the "aqua-planet", i.e. a virtual planet wholly covered with ocean of fixed surface temperature. The context and aim of the APE are fully discussed in Blackburn and Hoskins (2012), where the history and the position of idealized AGCMs (atmospheric general circulation model) experiments in the framework of atmospheric research in general are also stated. The setup of aqua-planet was first employed purposefully by Hayashi and Sumi (1986) in order to find the "natural" behavior of tropical atmospheric convection. They succeeded in identifying the hierarchy, or its substitute in low resolution model employing cumulus parameterization, that includes cloud clusters, super cloud clusters, ISV, tropical cyclones and double ITCZ. One might regard this setup is trivial or easy one because it is free from complex treatment of land surface and associated hydrology and/or vegetation schemes. However, it presents a unique and difficult challenge to AGCMs; being free from the external forcing provided from the inhomogeneity of underlying surface, the model atmosphere have to determine its behavior by itself, and hence both of the strength and the weakness of models are exposed clearly. In fact, as early as at the beginning of 1990's, it has been clarified that the choice of cumulus parameterization strongly affects several fundamental properties of AGCM such as the behaviors of tropical disturbances (Numaguti and Hayashi 1991a) or the structure of ITCZ (Numaguti and Hayashi 1991b).

The present paper describes the behavior of equatorial precipitation structures in CONTROL experiments conducted in the APE (Neale and Hoskins 2000). Among the series of classes of the hierarchical structure of tropical precipitation convection, we will focus our attention to the "intermediate" scale structure, i.e., convectively coupled equatorial waves (Kiladis et al. 2009), because of the following reasons in particular. The first reason, which is the most trivial, is that the smaller classes, i.e., individual cumulonimbi and mesoscale systems, are below the resolvable scales of most of the AGCMs participating in the APE. The second reason, which is also trivial, is that the larger classes, i.e., ISV, the convection centers and the ITCZs, are presumably strongly affected by the present idealized, unrealistic setup of aqua-planet. We should suspect that the behaviors of the models by themselves are unknown. It might be possible that the mechanism governing the ISV, if exist, obtained in the present setup is different from that of the ISV in the real atmosphere. The larger scale features should be examined from a wider perspective elsewhere (see, for instance, (Nakajima et al. 2011)). The third reason, which is the most important, is that, as will be shown later, the behaviors of convectively coupled waves in the models in the APE display rich variety possibly depending on the choice of cumulus parameterization employed. The examination of variety of the properties of convectively coupled equatorial waves (CCEWs) in the APE should enhance our knowledge on the underlying mechanism governing the CCEWs in coarse resolution AGCMs, which would lead us to the guiding principles on how to tune cumulus parameterization so as to better represent the behavior of the real atmosphere.

Among the CCEWs, we further confine our attention to Kelvin waves, equatorially symmetric westward gravity waves, and disturbances presumably advected westward by the background wind. These categories of CCEWs partially overlap with those examined in the wavenumber-frequency spectral analysis of observational data by Wheeler and Kiladis (1999). In other words, we exclude equatorial Rossby waves with especially large longitudinal scales and all of the equatorially asymmetric waves from our attention. In these disturbances, divergence is absent or weak at the equator (Yang *et al.* ,2007a). Consequently, it is expected that they are not strong in the experiments with CONTROL SST, where the distribution of SST has a rather sharp peak at the equator and the ITCZs are mostly confined to the equator (Blackburn *et al.*, 2012a). The properties of these disturbances should be examined elsewhere including the comparative analysis of the experiments with the other profiles of SST, two of which have more broad peak profiles.

The present paper is organized as follows. Section 2 will explain the setup of experiment. Because details of the APE project are given elsewhere (Blackburn and Hoskins,2011), only brief summary will be presented. Section 3 will present the methods of analysis. Section 4 will compare gross feature of CCEWs in the APE models. Section 5 will compare the composite structure of three categories of CCEWs produced from the regression analysis of spectrally filtered time series from the several selected models. Discussions and conclusions will be given in the last two sections.

2. Setup of Experiments

The experiments to be examined in this paper is the CONTROL case of the APE. As for the details not touched here, readers are referred to the context paper (Blackburn and Hoskions 2012) or the original proposal paper

(Neale and Hoskins 2000). The SST distribution is zonally uniform and fixed in time. The meridional structure is shown in Fig. 1. The SST profile is characterized with a rather sharp single peak located at the equator and north-south symmetric. The latitudinal gradient is steep from subtropics to midlatitude, whereas it flattens in high latitude region. Reflecting this character, climatological subtropical and mid-latitude jets effectively merge to form a single very strong jet located in subtropics.

In the APE archive, the results of 17 AGCM runs from 15 groups are accumulated. A brief summary of the specification of the models is given in Table 1. Among these, 7 groups provided more detailed time series on additional model variables for 8 runs, from which we obtain the composite structures as presented later. It is worth mentioning that even the subgroup for which composite analysis is performed contains a wide variety of spatial resolutions and cumulus parameterizations. More complete specifications are given in the APE-ATLAS (Williamson et al. 2011) to which readers are referred to.

Table 1

Fig. 1

3. Methods of analysis

3.1 Data

The data used in this study are the 6-hourly one year time series ("TR") of CONTROL experiments and the "additional transient time series" containing multilevel model variables of the following seven AGCM runs, AGUforAPE, CSIRO_std, ECMWF05, ECMWF07, GSFC, LASG, and NCAR. In the present paper, we mainly examine the latter data. The former contain model variables on very limited model levels, and are only consulted in order to check the representativeness of the seven model runs focused in this study among all of the AGCM runs. The variables we examined are zonal wind, meridional wind, vertical velocity, temperature, geopotential height, specific humidity, and, precipitation flux. In addition, temperature tendency due to parameterized convective process and that due to resolved condensation are used in the composite analysis of disturbances. Note that data for temperature tendency terms of CSIRO_std and resolved condensation of LASG are missing.

3.2 Hovmëllor plots and wavenumber-frequency spectra

In section 4, we show plots of time evolution ("Hovmëllor" plots) and wavenumber-frequency spectra of precipitation along the equator. For the models that do not have grid points on the equator, the averaged data of the two grid points nearest to the equator of the both hemispheres are used instead. Wavenumber-frequency spectra are obtained by the following procedures. (i) From the original 1-year time series of each model run, ten time series of the period of 90-days which begin at every 30 days from the beginning of the year are extracted. (ii) From each of the 90-day segment, linear trend, which is estimated using least square fit, is subtracted. (iii) Double Fourier transform is executed to obtain wavenumber-frequency spectrum of each of the segments. (iv) All of these wavenumber-frequency spectra of the ten 90-day segments are averaged to obtain the final estimate of the wavenumber-frequency spectrum of precipitation of each model.

In addition to the wavenumber-frequency spectra, we present the "enhanced" power spectra of the meridionally symmetric component of precipitation within 5 degree latitudes around the equator. The method to obtain the enhanced spectra basically follows that used in Wheeler and Kiladis (1999). (i) Time series of north-south symmetric component of precipitation is made for each latitude. (ii) Wavenumber-frequency spectra of this time series is produced in the same way as explained in the previous paragraph. (iii) Thus obtained power spectra for all latitudes within 5 degrees from the equator are averaged. (iv) The averaged spectra are divided by their "background" spectra which are obtained by applying 1-2-1 smoothing

40 times in wavenumber and frequency space.

3.3 Wave-type filtering

In section 5, we examine the structures of precipitation disturbances at the equator distinguishing the types of relevant equatorial disturbances. The method of separation basically follows that in Wheeler *et al.* (2000). We focus three types of convectively coupled equatorial disturbances; Kelvin (n=-1), westward inertio gravity (n=1), and "advective" components (hereafter these three components are referred to as K component, WIG component, and AD component, respectively). The last one has been referred to as "TD-type" component in Wheeler and Kiladis (1999). In the wavenumber-frequency domain of TD-type component, Yang *et al.* (2007a) identified equatorial Rossby waves modified by the Doppler effect due to easterly basic flow. However, the ITCZs appearing in the CONTROL experiment in most models are sharply concentrated at the equator (Blackburn et al. 2012a), so that the disturbances in the wavenumber-frequency domain corresponding to TD-type or "Doppler shifted Rossby waves" do not necessarily accompany vorticity. Association of vorticity is an indispensable character of tropical depressions (TD) or Rossby waves. From this reason, we choose the name of "advective component" instead.

The procedure for isolating each of the three types of components again basically follows that of Wheeler *et al.* (2000). (i) We perform double Fourier transformation of the three dimensional time series of the variables to be analyzed in longitude and time. (ii) We adapt the wavenumber-frequency spectral coefficients to those corresponding to the three types of disturbances by passing through the wavenumber frequency domains whose specifications are described below. (iii) We perform inverse double Fourier transformation of the filtered wavenumber frequency coefficients to obtain the three dimensional time series of variables representing each of the three types of disturbances. The definitions of the filters for the three disturbance types are shown in Fig. 2.

The range of equivalent depth associated with the filter for K component is broader than that in Wheeler and Kiladis (1999) where the range between 8m and 50m is employed. By the present choice, we intend to cover the wide variety of signals along around the Kelvin wave dispersion curves appearing in the various APE runs. In each of the APE runs, however, the range of the equivalent depth of its dominant K component is much narrower, as will be presented later. The domain of AD component is chosen considering following constraints. First, the lower bound of the westward propagating zonal wavenumber is selected to be four so as to avoid possible "contamination" by the disturbances of the type of planetary scale Rossby waves. Second, the upper bound of the frequency is set be 0.5 d^{-1} so as to avoid the overlap with WIG component. Third, the lower and upper bounds of characteristic velocity are selected to be 2.5 m/s and 12 m/s, respectively, so as to cover wide variety of possible disturbances that will fall in the category of "advective component" appearing in the various APE runs. The domain for WIG component follows that used in Wheeler and Kiladis (1999).

3.4 Composite structure

In Section 5, we present composite structure of K, WIG, and AD components along equator appearing in each of the seven AGCM runs. The composite structure is obtained by performing (simultaneous) regression analysis of the time series of model variables filtered through one of K, WIG or AD filters described in the previous subsection. Thanks to the idealized zonally symmetric configuration of the CONTROL experiment of the APE, the procedure of regression is quite simple. We extract a time series of a filtered model variable (*predictand*) at a height and a latitude, and shift the extracted data longitudinally by a certain zonal length, and calculate the slope of linear regression of the shifted time-longitude data against filtered precipitation at the equator. By repeating this procedure for all latitudes, heights, and zonal shift lengths, we can obtain the composite three-dimensional structure of the model variable for the disturbance of the filter used. We will not perform the lagged regression analysis, but averaged temporal evolution of traveling disturbances is, to some extent, expected to be captured as the zonal structure of the simultaneous composite. The details of the temporal evolution may be of interest, but it is left for future research.

It should be borne in mind that the magnitude of the regression slope of a particular variable at certain position for a particular model does not necessarily represent the intensity of the model variable actually realized in the model; it depends on the intensity of the filtered rain rate along the equator realized in the model, which varies significantly on different models as will be shown shortly below. The units of the regression slope are the units of the predictand per unit rain rate. However, for convenience, we multiply the values of the regression slope by a normalization intensity of precipitation, which is 0.0001 $[kg \cdot s^{-1} \cdot m^{-2}]$, and represent all predictand with their original units. Fig. 2

4. Behavior of equatorial precipitation in the APE models

4.1 Hovmëllor plots of equatorial precipitation

Fig. 3

Fig. 4

Fig. 5

Temporal evolution of precipitation at the equator of each model is shown in Fig. 3, where one can find quite a wide variety of representations of the hierarchical structure of equatorial precipitation among the different models. The calculated equatorial precipitation features seem to depend on both of the physical processes and the spatial resolution. For example, the higher resolution models such as DWD, ECMWF, FRCGC, CSIRO exhibit fine spatial structures, which cannot be observed in the lower resolution models, such as AGUforAPE, CGAM etc. The results of ECMWF_05 and ECMWF_07 are interesting. They have the same resolution but slightly different cumulus parameterizations, and show considerably different behaviors. The variety exemplified by the APE models is so widespread that it is difficult to describe meaningfully how the behavior of one model differs from that of another. So we only point out several noteworthy features.

In some models, eastward propagating planetary scale signals, whose propagation speeds are not very different from that of ISV in the real atmosphere (Madden and Julian 1994), are notable but with different intensity. FRCGC, i.e., NICAM run shows the most prominent eastward propagating signal as was described in Miura *et al.* (2005) and Nasuno *et al.* (2008). It is also evident in the results of K1Japan, two versions of UKMO, and two versions of ECMWF, but the intensity or detailed structures differ considerably. On the other hand, such eastward propagating low wavenumber signal is weak or absent in AGUforAPE, NCAR, and CISRO-old. In spite that these models are common in lacking notable eastward propagating signal, they differ significantly; precipitation in NCAR is generally weak and rather uniform, whereas that in CISRO-old is generally intense, and that in AGUforAPE is organized in westward propagating structures.

If we focus on smaller scale features, precipitation occurs near the "grid scale", i.e. nearly the smallest scale resolvable in all models in general. However, the behavior of grid scale precipitation varies significantly. The life time of such grid-scale precipitation varies among models ranging from about one day to nearly ten days. Moreover, the direction of migration of those grid scale precipitation structures also differ among models; those in AGUforAPE and MIT move generally westward, those in ECMWF05 and GFDL are nearly stationary, and those in UKMO, K1JAPAN, ECMWF07, DWD, and CSIRO move generally eastward.

4.2 Wavenumber-frequency spectra of precipitation

In contrast to the extremely rich variety in the appearance of equatorial precipitation in longitude time plot, the wavenumber-frequency spectra of the equatorial precipitation of 17 model runs (Fig. 4) exhibit some degree of similarity. The most common feature is the eastward propagating signal. In most models, the dominant power of the eastward propagating signals is distributed mainly along respective dispersion relation of equatorial Kelvin wave mode, although the intensity, characteristic equivalent depth, and dominant zonal wavenumber differ among the models. The identification of these signals as the equatorial Kelvin wave type is supported by the composite analysis of its spatial structure, which will be shown later.

The eastward propagating signal in NCAR is, however, somewhat different from those in other models; the dominant wavenumber, 5–10, is much larger than those in other models, 1–5. Moreover, the strong power seems to be distributed along the dispersion curve of n=1 eastward inertio gravity wave mode . Strangely, the wavenumber-frequency spectrum of mid-tropospheric vertical velocity (not shown) exhibits much weaker wavenumber dependence, so that the ratio of the intensity of precipitation to the intensity of vertical velocity, which might be interpreted as the gross sensitivity of the response of the latent heating to the grid scale ascent, strongly depends on wavenumber; precipitation is much more sensitive to vertical velocity in zonal wavenumber 5–10 than in zonal wavenumber 1–5. In the results of other models, there are not such distinct variation of sensitivity, and their magnitudes are more or less similar to that for the signal around wavenumber 5–10 of NCAR. It should be also noted that the reduced sensitivity of precipitation to vertical velocity in NCAR is observed only near the equator. This latitudinal dependence may be related to the latitudinal profile of ITCZ; NCAR is characterized with distinct "double ITCZ" structure, but most of other models in the APE are characterized with "single ITCZ" for the CONTROL SST profile. These evidences suggest that the eastward propagating signals in NCAR bear some character of eastward propagating inertio gravity wave with equivalent depth of about 12 m. However, as will be shown later, its composite structure is not very different from that of equatorial Kelvin wave.

In contrast to more or less common emergence of Kelvin wave type signals, the intensity and the spreading of "background component" vary much more drastically among the models. They reflect both the climatological structure of ITCZ and the structure of precipitation events. As is described in Blackburn *et al.* (2012a), the mean precipitation intensity at the equator varies over a factor of 3 among the models, and, as will be shown in the next section, the models with the larger mean precipitation intensity exhibit the larger power of over-all variance of precipitation. The wavenumber and frequency bandwidths are, from the definition of Fourier components, related to the degree of concentration of precipitation in the real space. More widespread background component found in DWD, ECMWF05, LASG, and FRCGC reflect more concentrated grid-scale precipitation structures as is recognized in Fig. 3.

It is interesting that, in most models, westward component extends to the higher frequency than eastward component does. Yang *et al.* (2009) indicate that similar feature of wavenumber-frequency spectrum of precipitation is found in Hadley center models and the observation of real atmosphere. The Doppler effect due to low level background easterly wind may be the origin of the east–west asymmetry, but further study is required to clarify the issue.

Intricate features can be seen more clearly in Fig. 5, where the signal enhancing technique of Wheeler and Kiladis (1999) is employed on those wavenumber-frequency spectra. The westward propagating background component are divided into two components. One is called, following the notation of Wheeler and Kiladis (1999) used for observed OLR (outgoing longwave radiation), "inertio gravity wave', or WIG, component whose signals are found in the region along dispersion curves of westward inertio gravity waves. The other is called "advective" (AD) component in this paper because they are generally distributed around straight lines passing through the origin in the wavenumber-frequency space, which indicates that disturbances are advected by background easterly winds. However, the actual relationship between the propagation speed of AD component and mean zonal wind is not straight forward as will be discussed in Section 6.1(c).

The behaviors of WIG components exhibit significant variety among models, although to a smaller degree than for those of AD components. In AGUforAPE and CGAM, the WIG signal is very weak, while it is distinct in LASG and K1JAPAN. In GSFC, the WIG signal is apparent in the enhanced power spectrum (Fig.5(j)), although the absolute intensity is not large (Fig.4(j)). Note that not only the intensity but also the distribution varies over the wavenumber-frequency space; the signals cover a wide range of wavenumber in LASG (Fig.4(l)) and K1JAPAN (Fig.4(k)), while the higher wavenumber signals can be noted in GSFC (Fig.4(j)). It is also worth noting that there is a gradual change of the characteristic equivalent depth of WIG component as wavenumber varies; WIG component of the larger scale tend to have the shallower equivalent depth. The most clear example is LASG (Fig.5(l)). This tendency suggests that the strength of coupling between convective heating and large scale convergence associated with WIG component might depend on the characteristic period of disturbances and result in the varying degree of “reduced stability” effect discussed by Gill (1982).

Because of the idealistic and clean setup of the APE project, one can easily recognize several types of planetary scale disturbances other than the convectively coupled equatorial waves and advective signals. One is the quasi-stationary wavenumber five signal. Most prominent example can be found in the result of NCAR (Fig4(o), Fig5(o)). Together with the ten-day period wavenumber six component nearby, it seems to be associated with the midlatitude baroclinically unstable waves like those examined by Zappa *et al.* (2011). Another example is the clear appearance of diurnal and semi-diurnal migrating tides (Woolnough et al. 2004). Additionally, we can find several types of normal mode waves which include the counterparts of those observed in the real atmosphere such as the 33-h Kelvin wave of Matthews and Madden (2000) and the $n = 0$ mixed-Rossby gravity mode and the $n > 1$ Rossby modes of Hendon and Wheeler (2008). These features are only marginally identifiable in the wavenumber-frequency spectra of precipitation, but are more easily confirmed in the spectra of zonal wind or surface pressure (not shown here). Among these waves, the representation of the 33-h Kelvin wave is found to be sensitive to the vertical resolution and/or the upper boundary conditions of the model, whereas that of other types of planetary scale disturbances mentioned above is less sensitive. The description of those waves is left for future research.

In many of the experiments, tidal signals significantly modulate the signals of tropical precipitation associated with the Kelvin or AD component significantly. Such modulation results in high frequency, low wavenumber component that sometimes overlaps the wavenumber-frequency domain of WIG and/or the region of eastward inertio gravity wave modes. Most clear example that the modulation of K component can be observed is that of UKMO (fig. 5(p,q)); the signals going through (wavenumber, frequency) $= (-5, 0.9)$ and $(-10, 0.6)$ in the wavenumber-frequency domain of WIG component are the projection images of the modulation of those for K component.

5. Spectral filtering analysis

As described in the previous section, there is a prominent variety in the space-time structures of equatorial precipitation calculated by the APE models. It it highly probable that various different choices of discretization schemes, spatial resolution, and implementations of physical processes among the models result in the variety of model behavior. However, it is a quite difficult task to point out one or more items that may cause one or more particular differences in such structures. Before any progress be made, it is necessary, at least, to describe the circulation structures associated with the characteristic space-time structures of equatorial precipitation, and differences among them.

As an attempt to describe systematically the various behaviors of equatorial precipitation in the APE models, we decompose the time series data of variables produced by each model into the contributions of Kelvin, WIG, and AD components, construct composite structures of them, and compare the characteristics of composite disturbances. The experiments to be analyzed are the subset CONTROL runs, where detailed transient data are additionally submitted. They are AGUforAPE, CSIRO, ECMWF05, ECMWF07, GSFC, LASG, and NCAR. Although the spectral property of each component differs among models, we use the same definition of the filters for each model. As a result, some of the dominant spectral power are excluded from the composite for some models; most suffering from this is WIG component in LASG where the contribution from the low wavenumber region is out of the range. However, by this choice of the filters, we prioritize the uniform application of filters to the results of all of the models to be compared over the completeness of coverage of the three spectral components appearing in the results of each model. The wavenumber-frequency domains of three kinds of filters are shown in Fig. 2.

5.1 *Intensities of Kelvin, WIG and AD components*

Fig. 6

Fig. 7

Before examining the spatial structure of each component, we compare the intensities of three components of the additionally contributed seven APE models. Fig. 6 shows the variance of equatorial precipitation calculated from the time series with K, WIG, and AD filters; the absolute values (Fig. 6(a)) and the values normalized by the variances of original, unfiltered time series of precipitation of corresponding models (Fig. 6(b)). Fig. 7 is a scatter plot showing the relationship between the mean precipitation squared and the two kinds of precipitation variances; shown by circle is the total variance, i.e., the variance of the original time series of each model, and shown by square is the sum of the variances of the three filtered components. It is evident from Fig. 6(a) that the intensities of all components are strongly model dependent. LASG and ECMWF05 are members that exhibit most intense disturbances, whereas NCAR, GSFC, and CSIRO are those with weakest. As for the intensity sum of K, WIG, and AD components, that of ECMWF05 is about 30 times as large as that of NCAR. (see also those plotted by squares in Fig. 7).

In Fig. 6(b), we can point out two aspects commonly noted among the models. First, the sum of the three components contributes to roughly about ten percents of the total variance of precipitation of each model. the contribution other than those three components is not at all negligible. Second, WIG component is weakest in the three kinds of disturbances. However, the relative intensity of variances between K component and AD component varies largely among the models. There is a weak negative correlation between the intensities of K and AD components. AGUforAPE and ECMWF07 show contrasting features; AD component dominates in AGUforAPE, whereas K component dominates in ECMWF07. It is an important issue to understand how the magnitudes of contributions of these three components to the total variance of precipitation are determined. However, it is left for future studies.

It may be worth mentioning that both the unfiltered total variance and the variance sum of the three components are well correlated with the average precipitation intensity (Fig. 7). Total variance, for instance, is proportional to the cube of the average precipitation rate. LASG and CSIRO are outliers exhibiting the larger and the smaller variance expected from the tendency shared by the models, respectively. The variety of total variance corresponds to the variety of the probability distribution function (PDF) of precipitation. As shown in Fig.18 of Blackburn *et al.* (2012a), in the models with the larger variance, EC05 and LASG, the PDFs have long tails in the strong precipitation compared with the PDFs in the models with the smaller variances, e.g., NCAR, GSFC, or CSIRO. One may imagine that variance is the larger in the models with the higher spatial resolution.

However, it is not true; LASG, in which the total variance is very large, is one of the models with the lowest horizontal resolution, and, EC05 and EC07 differ drastically in the total precipitation variance in spite of their identical horizontal resolution. The PDF of CSIRO does not have a long tail, although its mean precipitation rate is not small. It is more plausible that the variance is more strongly governed by cumulus parameterization. This issue is also left for future research.

5.2 Composite structure of Convectively Coupled Equatorial Waves

Hereafter, the composite structures associated with K, WIG, and AD components of the seven APE models are examined. As was written in section 3, the composite structures are derived from the regression of corresponding filtered variables to the symmetric component of filtered precipitation intensity at the equator. The variables in the following figures are scaled for 0.0001[Kg/s m^2] precipitation anomaly at the reference latitude, 180 degree longitude. Note that the intensities of composite disturbances presented in the following figures do not represent the intensities of those disturbances emerging in the models; only their structures matter.

a. *Composite structure for K component*

Fig. 8 Fig. 9 Fig. 10 Fig. 11 Fig. 12 Fig. 13 Fig. 14

The composite structures for K component are presented in Fig. 8–14. Fig. 8 shows the horizontal structures of precipitation and horizontal wind at the height of 925hPa. In all models, precipitation anomalies are well confined near the equator. However, the latitudinal extents somewhat differ; in ECMWF05 and LASG, they are sharply confined around the equator whereas in AGUforAPE, ECMWF07, and NCAR, they are broad. Generally, the north-south extent corresponds to the width of the ITCZ in each model (Blackburn et al. 2012a). The longitudinal structures also differ among the models; in LASG and ECMWF05 and GSFC, they are confined around the precipitation peak, while in AGUforAPE and ECMWF07, they are broader. In NCAR, precipitation anomaly has a wave-like variation with the wavelength of about 6000km, and associated with off-equatorial signal which is delayed with 10 degrees. Similar off-equatorial signal can be found also in GSFC. Note that both of the two models are characterized with distinct double ITCZ structure (Williamson et al. 2011). The horizontal wind structures deviate from that expected from the shallow water Kelvin wave (Matsuno 1966); the magnitudes of meridional flows are not very different from those of zonal flows. Convergence of meridional wind commonly occurs at almost the same location as that of zonal wind. Among the seven runs, AGUforAPE exhibits a most deviated horizontal wind structure. Generally, low level horizontal wind driven by condensation heating tends to be confined around the condensation heating (precipitation) area, as is typically indicated by CSIRO, ECMWF05, ECMWF07, and LASG (Fig. 8(b), (c), (d), (f)). However, AGUforAPE (Fig. 8(a)) shows wide spread wind response especially to the west of condensation heating. We can recognize anticyclonic circulations which seem to extend beyond the range of the figure to the subtropical latitudes.

Fig. 9 shows the horizontal structures of geopotential and horizontal wind at the height of 850hPa. The horizontal structures of most models are similar to that of shallow water equatorial Kelvin wave (Matsuno 1966) in the sense that zonal component dominates in the wind field and geopotential height and zonal wind are positively correlated and confined around the equator. Wind convergence appears near the precipitation maximum in all of the models. However, precise location of convergence varies among models; it resides 5-10 degrees to the east of the the rainfall maxima in AGUforAPE, CSIRO, ECMWF05 and ECMWF07, about 2 degrees to the east in GSFC and LASG, and about 2 degrees to the west in NCAR.

One of the features at the level of 850hPa that deviate from the structure of Kelvin wave, we can recognize significant meridional wind perturbation near the precipitation maximum for all models. It may be worth mentioning that the strength of meridional wind perturbation depends on the choice of variable for the key of regression; the composite horizontal structure based on the regression to low level zonal wind at the equator (not shown here) exhibits much weaker meridional wind, displaying the larger degree of similarity to a shallow water Kelvin wave.

The structure of AGUforAPE (Fig. 9(a)) exemplifies a peculiar structure of deviation from that of Kelvin wave. Its zonal wind perturbation is strongly confined in the vicinity of the equator compared to that of geopotential height. The meridional wind perturbation, on the other hand, seems to originate in the higher latitudes in the same way as observed at the surface level (Fig. 8(a)). By inspecting Fig. 9 and also Fig. 8 more carefully, we can point out that NCAR also show somewhat peculiar features. First, the longitudinal extent of the composite structure is small compared to others; the others show one pair of high and low pressure anomalies along the equator while NCAR shows one and half. This feature is also confirmed in the power spectra of equatorial precipitation (Fig. 4); signals with wavenumber 5–10 are dominant in NCAR, whereas those with the smaller wavenumber are dominant in the other models. Second, the precipitation anomaly exhibits a significant meridional phase difference; the longitude of maximum precipitation at the latitude of the ITCZ is located at about 10 degree to the west of that at the equator. This horseshoe like structure can be constructed as a superposition of the horizontal structures associated with equatorial Kelvin wave and eastward inertio gravity wave, the latter being shifted by about 5 degrees to the east of the former. Coexistence of those two types of wave structures is consistent with the dominant precipitation signals in the wavenumber-frequency space (Fig. 4(o) and Fig. 5(o)), where intense power appears along the dispersion relation of not only Kelvin wave but also eastward inertio gravity wave having the equivalent depth of about 10 m, Also observed is that the horizontal wind structure at the surface level shown in (Fig. 8(g)) resemble that of eastward propagating inertio gravity wave. The composite horizontal structure of K component in NCAR seems to include both of the features of eastward propagating inertio gravity waves and Kelvin waves.

In contrast to the resemblance among the models observed in the surface and the lower troposphere, there is considerable model dependence in the upper tropospheric structures. Fig. 10 shows the horizontal structures of geopotential and horizontal wind at the level of 250hPa for K component. The divergence of zonal wind perturbation around the maximum of precipitation that is the feature expected for the so called first baroclinic thermal response of Kelvin wave type without background wind is found only for LASG and NCAR. In ECMWF07 and GSFC, the areas of zonal wind divergence are found as far as 1500–2000 km to the east of the precipitation maximum. In AGUforAPE, CSIRO, and, ECMWF05, zonal winds are convergent at the precipitation maxima; the horizontal divergence that is required as the continuation of the upward flow at the precipitation maximum is accounted exclusively by the divergence of meridional flow. Additionally, significant vortical perturbations are notable in the subtropics, although the phase of the vortice relative to the location of the precipitation maximum varies among the models.

The diversity in the upper troposphere appears because the phase velocities of the signals of K component, which are typically 10 $\sim$ 30 m/s, are not very different from the zonal mean zonal wind in the upper troposphere in the tropical and subtropical regions in the models. There are mainly two effects caused by the existence of background westerly wind. One is that intensity of thermal response of Rossby wave type changes greatly according to the intensity of background westerly. The other is that the effective value of equatorial β including the background wind term $-\overline{u}_{yy}$ tends to decrease, since the background westerly tend to reach zero potential vorticity field around the equator (Sardeshmukh and Hoskins 1988). The response structure could be quite sensitive to the subtle difference of the structure of basic wind and heating at the precipitation anomaly. The structure of the vortical perturbation associated with K component in the different models are presented in Appendix for interested readers.

Fig. 11 shows the vertical structures of temperature, zonal wind, and vertical velocity along the equator for K component. We note that temperature and vertical velocity anomalies in ECMWF05, ECMWF07, LASG, and NCAR, have westward phase tilt being consistent with wave-CISK theory. At the same time, we should emphasize that the vertical structure of temperature anomaly displays a wide variety among the models. We can notice at least four types of temperature perturbations among the models; a signal of the first baroclinic mode extending whole depth of the troposphere, a signal of the second baroclinic mode which has two maxima of amplitude in the troposphere with longitudinal phase shift to each other, a thin signal at around 600hPa that is associated with the melting of ice phase hydrometeor, and another thin signal near the surface possibly associated with the evaporation of raindrops. In each of the models, the four types of temperature signal appear in different combination, intensity, and phase relationship, resulting in the wide variety of the temperature structure.

Fig. 12 shows the vertical structures of specific humidity, zonal wind, and vertical velocity along the equator for K component. As a common feature in most models, the humidity field is characterized with a "slant" structure; lower troposphere is moist to the east of the rainfall anomaly, and dry to the west, whereas middle and upper troposphere is dry to the east and moist to the west. In GSFC, however, the longitudinal distribution of humidity anomaly in the lower troposphere around 700–925hPa has the opposite sign to those in the other models; humidity of GSFC is dryer (more moist) to the east (west) of the rainfall anomaly. Another common feature is the existence of a shallow dry region near the surface to the west of the precipitation anomaly, which could be a result of downdraft driven by the cooling associated with, presumably parameterized, evaporation of raindrops.

The vertical structures of circulation at the equator shown in Fig. 11 and Fig. 12 vary considerably among the models. In the majority of the models, the first baroclinic mode structure dominates in the vertical velocity fields, although the location of upward motion does not necessarily corresponds to the area of upper level zonal wind divergence because of the significant contribution of meridional wind divergence mentioned above and also shown later. In most models, the contribution of the second baroclinic mode structure can be noted by the existence of the westward phase tilt. Examples are found in ECMWF05, ECMWF07, LASG, and NCAR. The composite disturbance of GSFC has one notable feature; a significant downward flow of cool air is found in the lower troposphere to the west of the maximum of precipitation. This is a structure somewhat similar to the mesoscale downward flow that develops below anvil clouds of mesoscale precipitation features (Houze and Betts 1981). However, the zonal extent in Fig. 12(f) is too broad to be regarded as mesoscale; this feature could be explained as a cumulative effect of more compact cold downdrafts found in AD component, which will be presented later.

The composite structures of temperature tendency due to parameterized convection (referred to as DT_CONV hereafter) and those due to resolved clouds (referred to as DT_CLD hereafter) at the equator of K component are shown in Fig. 13 and Fig. 14, respectively. In all models, DT_CONV is zonally well confined. In NCAR, regions of significant negative values are observed to the west and to the east of the center of precipitation anomaly. However, recalling that precipitation itself has a zonally wavy structure (Fig. 8(g)), they directly correspond to in situ precipitation anomaly. On the other hand, the vertical structure of DT_CONV is strongly model dependent. In LASG, it is distributed mainly in the lower troposphere. In AGUforAPE, ECMWF05, and, ECMWF07, the distributions of DT_CONV are mostly confined above the freezing levels, whereas those in GSFC and NCAR, they have deep structures extending to both of the lower and the upper tropospheres. In ECMWF07, there is a region of cooling near the surface, presumably resulting from rain evaporation.

The distributions of DT_CLD are strongly model dependent, not only in their vertical structures but also in their zonal structures. In AGUforAPE and ECMWF05, DT_CLD is zonally confined and the vertical structures are similar to those of corresponding DT_CONVs. In ECMWF07, GSFC, and presumably NCAR, the distributions of DT_CLD spread much more extensively in the zonal direction than those of precipitation. In ECMWF07 and GSFC, the distributions are characterized by the second baroclinic mode structure; in the lower troposphere, heating is positive to the east of the center of precipitation anomaly, and negative to the west nicely representing the cooling due to evaporation of stratiform precipitation. It should be noted that the cooling area extends about 3000 km to the west of the center of precipitation anomaly, which is much wider than the typical extent of "mesoscale precipitation features" (Houze and Betts 1981). As a result, overall structure of the heating is somewhat similar to "giant squall lines" observed in the upward motion area of Madden Julian Oscillation as described e.g. in Mapes *et al.* (2006). There are also shallow regions of cooling near the surface in ECMWF05, ECMWF07 and NCAR. Such cooling near the surface is absent in AGUforAPE.

In summary, the composite structures of K component have some degree of similarity to those of the equatorial Kelvin wave mode. This is especially true for the horizontal structure in the lower troposphere. The vertical structures, on the other hand, are shown to be strongly model dependent. It seems that the intensity of disturbances of K component in a particular model seems to increase as the increase of the similarity of the composite structure to the structure of the unstable wave-CISK mode. This point will be discussed in Section 6.

b. Composite structure for WIG component

Fig. 15
Fig. 16
Fig. 17
Fig. 18
Fig. 19
Fig. 20
Fig. 21

The composite structures for WIG component are presented in Fig. 15–21. Fig. 15 shows the horizontal structures of precipitation and horizontal wind at the level of 925hPa, and Fig. 16 shows the horizontal structures of geopotential and horizontal wind at the level of 850hPa. We can observe that the horizontal structures of geopotential and wind disturbances are similar to those of shallow water westward propagating equatorial gravity wave mode. For all models, there are clear dipole structures of geopotential anomalies aligned along the equator. The positive (negative) geopotential anomalies locate to the west (east) of the rainfall anomalies. The horizontal convergence anomalies also tend to appear about 5 degrees to the west of the centers of precipitation anomalies. Zonal and meridional wind components contribute about equally to the intensities of convergences. It may be noted that rainfall anomalies show wavy variation in AGUforAPE and LASG.

The structures of disturbances in the upper troposphere (Fig. 17) are, unlike the composites of K component, similar to those of the corresponding equatorial westward inertio gravity wave mode of a shallow water system. The signature of geopotential anomalies is opposite to that in the lower level (Fig. 16) except that the patterns are shifted to the east. The areas of horizontal divergence are located to the east of the precipitation maxima by $5 - 10$ degrees, being consistent with the eastward tilt of the vertical velocity anomalies shown later. The smaller degree of model dependence of the upper tropospheric horizontal structures of WIG component compared to those of K component can be understood considering the propagation direction. Disturbances of WIG component propagate westward and their doppler shifted phase velocities do not become small anywhere in the troposphere, while those of K component propagate eastward and their doppler shifted phase velocities become small in the upper troposphere as mentioned previously.

Fig. 18 and Fig. 19 show the vertical structures of temperature and specific humidity, respectively, superposed on zonal wind and vertical velocity along the equator of WIG component. In the same way as those of K component (Fig. 11 and Fig. 12), they exemplify wide diversity among the models. We may say that vertical velocity anomalies have some eastward phase tilt in many of the models, being consistent with wave-CISK theory. However, the structures of temperature anomaly are more complex than those often described as the first or the second baroclinic mode in simple theoretical models. Notable, but not necessarily common, features are the existence of thin structures at around the melting level and near the surface. An interesting feature observed in GSFC and LASG is that magnitudes of temperature, vertical velocity and specific humidity anomalies are large in the lower troposphere. Note that GSFC and LASG are the runs where WIG component is relatively active as indicated in (6(b)). However, the structure does not look similar to each other. A peculiar feature of GSFC is a pair of temperature anomaly in the lower troposphere; a warm area to the west and a cool area to the east of the precipitation maximum. It seems that vertical wind and temperature is positively correlated in GSFC, while westward tilt of anomalies below the middle of the troposphere is more evident in LASG. As for moisture anomaly, the longitudinal moisture contrast around the precipitation maximum is more evident in the lower troposphere than in the upper troposphere in ECMWF05 and ECMWF07. This contrasts with that for K component (Fig. 12(c) and (d)) where the moisture signal is stronger in the upper troposphere. CSIRO, where thin moisture structures can be observed in WIG component, also shows that the lower tropospheric moisture signal is stronger for WIG component than for K component. In GSFC and NCAR, shallow east-west contrast of humidity near the surface is notable. In ECMWF05, where WIG activity is remarkable as shown in 6(a), the intensity of the composite disturbance seems to be rather weak. However, since the plotted quantities are the coefficients of regression to the unit amount of precipitation, the structure of WIG component emerging in ECMWF05 becomes quite significant.

The composite structures of temperature tendencies due to parameterized convection, DT_CONV, and those due to resolved clouds, DT_CLD, on the equator are shown in Fig. 20 and Fig. 21, respectively. The structure of DT_CONV for WIG component in each model is generally similar to that of the corresponding composite for K component. If we compare carefully, however, the vertical distribution of heating for WIG component is shifted slightly to the lower altitudes. The structure of DT_CLD for WIG component in each model is also generally similar to that for K component, except that the zonal direction is reversed and the zonal extent is shortened to about one-third. We can point out for NCAR, as an example description of the difference between the structures of DT_CLD for WIG and K components, the difference of the distributions of rainfall. There appear only one pair of heating and cooling regions for WIG component (Fig. 21(g)) while there are one and half wavelength of heating and cooling regions in DT_CLD for K component (Fig. 14(g)). Correspondingly, the rainfall distribution of WIG component is more solitary, while that for K component is more wavy. The distribution of DT_CLD for WIG component should be associated with a rather solitary rainfall event. Indeed, the west-moist and east-dry structure of DT_CLD for WIG component can be recognized as an representation of shallow cloud activity preceding the updraft and the afterward evaporation of stratiform-type rainfall.

In summary, the horizontal structures of WIG component have characteristics similar to those of the equatorial westward inertio gravity wave mode even in the upper troposphere. However, the vertical structures of composite disturbances are shown to be strongly model dependent. As is clearly indicated for LASG (Fig.18(c)), there are models where the vertical structures are similar to those of the unstable mode of wave–CISK; tilted updraft and temperature fields, while, as indicated for GSFC, there are models where the areas of cold downdraft exist in the lower troposphere caused by stratiform-type precipitation activity, contributing generation of kinetic energy.

c. *Composite structure for AD component*

Fig. 22

Fig. 23

Fig. 24

Fig. 25

Fig. 26

Fig. 27

Fig. 28

Fig. 22 shows the horizontal structures of precipitation and horizontal wind at the level of 925hPa. In all models, the precipitation anomaly is confined both meridionally and longitudinally. The zonal extents for AD component are much smaller than those for K (Fig. 8) or WIG (Fig. 15) components. There are negative anomalies of precipitation to the east and west of the main positive anomaly in ECMWF05 and LASG. In NCAR, there are a pair of negative anomalies to the north and to the south of the precipitation maximum. Fig. 23 shows the horizontal structures of geopotential and horizontal wind at the level of 850hPa. The horizontal structures in the lower troposphere are strongly model dependent. In AGUforAPE, there is a pair of cyclones straddling the equator at around the longitude of maximum precipitation. More or less similar pair of cyclones can be noted also in CSIRO, but they are located closer to the equator. The pairs of cyclones in AGUforAPE and CSIRO are similar to the Doppler shifted equatorial Rossby waves in the analysis of Yang *et al.* (2007a,2007b). In ECMWF05 and ECMWF07, the geopotential anomalies at around the equator are weak. In ECMWF05, there is a low pressure anomaly on the equator at the maximum of precipitation, but, in contrast to the vorticity dominated flow in AGUforAPE, the lower level flow converges without intense rotational feature. In ECMWF07, the low level flow off the equator near the precipitation maximum is anticyclonic. In GSFC, the maximum of precipitation accompanies distinct high pressure and divergence, whereas a low pressure anomaly and convergence appear about 1,200 km to the east. To the north and south of the equatorial high and low pressure anomalies, flow exhibits anticyclonic circulation. In LASG, a low pressure area on the equator is located at the precipitation maximum, and convergent flow is observed just to the west. In NCAR, the equatorially confined geopotential feature is not well recognized. In contrast to the diversity of the horizontal structures in the lower troposphere described above, those in the upper troposphere (Fig. 24) are more or less similar to each other, being characterized with a compact high pressure anomaly at around the precipitation maximum from which horizontal wind diverges almost isotropically.

Fig. 25 and Fig. 26 show the vertical structures of temperature and specific humidity, respectively, superposed on zonal wind and vertical velocity along the equator of AD component. The vertical structures are extremely model dependent. AGUforAPE is unique in the presence of an intense lower level warm anomaly. ECMWF05 is characterized with a deep warm core through which an upright ascending motion exists. These two models are common in lacking the cool anomaly near the surface which appear in most of the other models. A lower tropospheric warm core exists also in CSIRO, but it exhibits a distinct surface cold signal. ECMWF07, GSFC, and NCAR are common in that the lower troposphere below the melting level around 600hPa is cool. ECMWF07 has a distinct cool region near the surface. The characteristics of the lower tropospheric vertical velocity at the precipitation maximum vary even in these three models; updraft dominates in ECMWF07, but it is almost absent in NCAR, and downward motion dominates in GSFC. In GSFC, there exists a distinct low level upward motion at around the level of 850hpa about 1,000-1,500 km to the east of the precipitation maximum, where positive heating anomaly of DT_CLD can be found as will be shown shortly below. LASG exhibits a cold anomaly in the low level, a warm anomaly around 500hPa, and a cold anomaly again near the tropopause; there is no feature corresponding to the thin cold anomaly around 600hPa found in most of the other models, presumably because the melting of icy hydrometeors is not considered in LASG. The vertical structures of humidity (Fig. 26) are characterized with the longitudinally confined positive anomalies at the location of precipitation, but their vertical extents differ among the models. In AGUforAPE and LASG, updraft covers the deep regions of moist anomaly. In the middle and upper troposphere, moist area appears also in other models, but in the lower troposphere, the humidity structures are much more model dependent.

The composite structures of temperature tendencies due to parameterized convection, DT_CONV, and those due to resolved clouds, DT_CLD, along the equator are shown in Fig. 27 and Fig. 28, respectively. The structure of DT_CONV in each model is generally similar to that in the composite of K or WIG component of the corresponding model. If we compare carefully, however, the vertical distribution of the heating is shifted slightly to the higher altitudes than for that of K or WIG component for all models. This difference is most notable in NCAR and GSFC. DT_CLD of AD component is zonally localized in most models, in contrast with the zonally extended structures of DT_CLD in K and WIG components (Fig. 14 for K and Fig. 21 for WIG components, respectively). However, GSFC is an exception in that DT_CLD is not localized; prominent low level heating and upper level cooling anomaly exist at about 1,300 km to the east of the precipitation maximum, where low level convergence and upward motion appear (Fig. 23(e) and Fig. 25(e)). In AGUforAPE and ECMWF05, the vertical structures of DT_CLD are similar to those of DT_CONV as in corresponding K and WIG components. In other three models, ECMWF07, GSFC, and, NCAR, the lower troposphere at the precipitation maximum is the region of cooling. The cooling of DT_CLD, which results presumably from the evaporation of stratiform, nearly cancels out the heating caused by DT_CONV in those models. The cancellation is consistent with the weak updraft in the lower troposphere of those models.

In spite of the widely different structures among the models described above, we can point out two common features shared in all models; the vertical motions are upright, and are localized around the precipitation maxima. These two points are in contrast with the structures of composite signals found for K and WIG components, both of which have significant tilting and broader zonal extent. The upright structure of the advective component suggests that it may not be a wave-CISK type instability but may be a CIFK (conditional instability of the first kind) type instability that drives AD component.

6. Discussions

6.1 Possible mechanism supporting each type of of disturbances

We try to point out possible mechanisms that determine how prominently disturbances of each component emerge in different models.

a. K component

Based on the composite structures of K component and the wavenumber-frequency spectra of precipitation of the APE models, we can point out that characteristics obtained by classical wave-CISK theory seems to be still useful in describing the structures of disturbances. In ECMWF05, ECMWF07, LASG, and NCAR, where K component is distinct (Fig. 4(f), (g), (l) and (o)), the vertical structures of the composite disturbances (Fig. 11(c), (d), (f) and (g)) are similar to those of the eastward propagating unstable equatorial Kelvin modes of wave-CISK (e.g., Hayashi, (1970); Lau and Peng, (1987); Chang and Lim, (1988)) and the observed convectively coupled Kelvin wave (Wheeler and Kiladis 1999). Namely, both temperature perturbation and vertical velocity are tilted westward as the increase of altitude, and in the upper troposphere, they are positively correlated. This positive correlation accounts for the energy conversion from available potential energy to kinetic energy. In NCAR, K component exhibits a similar structure except that the westward tilt of the temperature anomaly is not very large (Fig. 11(g)). However, recalling that the dominant wavelength of the K component disturbances in NCAR is much shorter than those of the three models above, this phase tilt is small but significant. As the wavelength is about 60° ($\sim$ 6,000 km; see Fig. 9(g) for example), the longitudinal difference between the mid tropospheric warm anomaly and the upper tropospheric warm anomaly, 12°, is as large as 1/5 of the wavelength. On the other hand, in the other models, where K component is not distinct, updraft and/or temperature anomaly lacks a proper vertical phase tilt expected from wave-CISK theory. In CSIRO, updraft is slightly tilted westward, but temperature anomaly is not tilted. In GSFC, temperature anomaly is tilted eastward. In AGUforAPE, the so called second baroclinic mode is significant in the temperature anomaly, and there is a strong negative correlation between upward motion and temperature in the lower troposphere, which is unfavorable for generation of kinetic energy.

It should be remarked that we are not claiming naive application of wave-CISK in its original form to the results be valid. In each model, the vertical profile of heating in the composite structure exhibits considerable longitudinal variation, which originates mainly from the contribution of the stratiform cloud process (Fig. 14). This situation of heating seems to be far from the assumption of wave-CISK where the vertical profile of heating is prescribed and its magnitude is proportional to low level convergence or updraft. Nevertheless, as is demonstrated by Nakajima *et al.* (2012) , the prediction of wave-CISK, e.g., the sensitivity to the vertical structure of cumulus heating, seems to remain basically valid even in GCMs where the vertical profile of heating is determined through rather complicated procedures. However, we could not go into further details at this point. More complete time series of model runs may be indispensable for examining and understanding the nature of coupling between waves and parameterized cumulus convection. In addition, it may be necessary to incorporate more sophisticated theories (e.g., Kuang, 2008; Andersen and Kuang, 2008), and comparison with cumulus resolving models (e.g., Kuang, 2010).

A delicate issue is to understand the emergence of eastward propagating signals in CSIRO, GSFC, and AGUforAPE. Although the disturbances of K component in AGUforAPE is not evident in the original power spectrum of equatorial precipitation (Fig. 4(a)), the enhanced power spectrum (Fig. 5(a)) suggests the existence of disturbances of K component. The signals of K component in GSFC and CSIRO are even more evident as shown Fig. 5(c) and (l). However, their structures do not seem to be consistent with those predicted by classical wave-CISK; they do not show clear westward phase tilt in the vertical direction. Actually, their heating profiles are not favorable for generating disturbances of the wave-CISK type. There is a region of cooling in the upper troposphere in AGUforAPE (Fig. 13(a)), and there is a large contribution from resolved clouds (DT_CLD) in GSFC (Fig. 14(e)). The reason why we can find disturbances of K component in those models are not clear. One possibility is the wind-induced surface heat exchange (Emanuel, 1987 and Neelin *et al.*, 1987), where no phase tilt of a disturbance is required. Another is a forcing from, or the interaction with the midlatitudes. As is presented in the Appendix, the structures of disturbances of K component are associated with vortical signals in the subtropical latitudes. Furthermore, supplementary analysis (not presented here) shows that non negligible correlation exists between the midlatitude meridional wind and the low latitude precipitation in most models. Some authors, for example, Zappa *et al.* (2011) and Straus and Lindzen (2000), investigated possibility of the midlatitude disturbances and the tropical convective activities. Confirmation of these considerations with the APE data is left for future research.

b. WIG component

Compared to K component described above, the relationship between the intensity and the structure of disturbances among different models is less clear. As for the absolute intensity, singnals of WIG component are noticeable in ECMWF05 and LASG (Fig. 6(a)). The composite vertical structures of these (Fig. 18(c) and (f)) show eastward phase tilt in temperature and wind disturbances, which is a feature common to westward propagating unstable modes of wave-CISK. We can also recognize similar tilted structures for WIG components in NCAR and ECMWF07 (Fig. 18(d) and (g)), although the intensities of WIG components for these are not very large.

As for the relative intensity normalized by the total variance of precipitation (Fig. 6(b)), LASG and GSFC are the models with large WIG components. Common features notable in these two models are intense temperature and vertical velocity perturbations in the lower troposphere (Fig. 18(e) and (f)). This combination may be preferable to activate coupling between gravity waves and convective activity. The composite disturbance of GSFC has a peculiar characteristics; to the east of the precipitation anomaly in the lower troposphere, there is a region of downdraft in the cold anomaly, which may help generation of gravity waves. This cool downdraft is presumably induced by the cooling due to the evaporation of stratiform rain (Fig. 21). The timescale of about 1 day and the horizontal extent of about 1000 km are not quite different from those of observed mesoscale precipitation systems (Houze and Betts 1981), WIG (Takayabu 1994b), or so-called “2-day waves” (Haertel and Kiladis 2004). However, it is not clear whether such seemingly superficial correspondence supports a particular parameterization of cloud processes.

c. *AD component*

AD component is significant in ECMWF05, LASG, and AGUforAPE, measured either by the absolute intensity or by the relative intensity normalized by the total variance of precipitation (Fig. 6). Before examining possible factors that contribute the high intensities of AD components in these three models, it is important to examine whether the disturbances of AD components in these models should be identified as "advective" in more strict sense. In the wavenumber-frequency spectra (Fig. 4 or Fig. 5), we can easily find that the signals of AD components in AGUforAPE and LASG have dominant phase velocities, respectively, while we cannot in ECMWF05. In AGUforAPE and LASG, the dominant westward phase velocities are about 10.3m/s and 7.7 m/s, respectively. They are reasonably close to the zonal mean zonal winds at 850hPa of the corresponding models, namely, 11.2 m/s and 8.3 m/s, respectively. The Hovmëllor plot for LASG (Fig. 3(l)) may give an impression of much faster phase velocity. However, this impression results from the superposition of faster disturbances of WIG component and slower disturbances of AD component. The coincidence of the zonal wind velocity and the phase speed suggests that the motions of disturbances in AD component of AGUforAPE and LASG are indeed governed by advection of certain physical variables.

AD component spectrum of ECMWF05, on the other hand, is scattered in a wide range with red frequency distribution in wavenumber-frequency space. Because of this wide bandwidth, a significant portion of power does fall within the defined spectral region of AD component. And hence, no characteristic velocity can be pointed out. However, disturbances of AD component in ECMWF05 requires more careful examination. In the Hovmëllor plot of precipitation (Fig. 3(f)), we can notice that intense grid-scale precipitation of ECMWF05 is not short-lived; it sometimes lasts for as long as about 5days. Looking into such cases closely, we can find that these grid-scale precipitation areas move very slowly; in some cases, they do not move at all throughout the 5 day lifetime. This slow movement is not trivial because it can hardly be explained by advection of physical variables by the zonal mean zonal wind, which is about -7.5 m/s at 850hpa in ECMWF05. Close examination reveals that those strong grid-scale convections tend to develop to the west of the low level zonal convergent area of intense disturbances of K component, where the low level westerly wind anomaly associated with the K component almost completely offset the zonal mean easterly winds. The advection by the local wind explains the behavior of grid-scale precipitations in ECMWF05 including their very slow movement. We can conclude that, as in AGUforAPE and LASG, AD component in ECMWF05 is presumably governed by advection of certain physical variables.

Now the issue to be examined is to identify the physical quantities that keep the identity of the disturbances of AD component. In AGUforAPE, one of the physical quantities seems to be water vapor mixing ratio, which exhibits a deep positive anomaly at the maxima of precipitation (Fig. 26(a)). The low level vorticity anomalies at the off equatorial regions around the precipitation maximum (Fig. 23(a)) may also contribute to keep the identity of AD component disturbances either as coherent vortices or as equatorial Rossby waves (Yang *et al.*, 2007a; 2007b). In LASG and ECMWF05, a positive moisture anomaly at the rainfall maximum is also found (Fig. 26(c) and (f)). However, we are less confident that the moisture anomaly serves as the memory variable to be advected, because the intensity of the moisture signal in LASG is weaker than that in AGUforAPE, and it is further weaker in ECMWF05. However, the weakness of the moisture signal in ECMWF05 is a result of mismatch between the characteristic phase velocity that define AD filter, 2.5–12 m/s, and the true motion velocity of the grid-scale precipitation in ECMWF05, which is almost zero, mentioned in the previous paragraph. It should also be reminded that the intensity of the composite signal is normalized by the intensity of precipitation anomaly; the precipitation signal in ECMWF05 is very strong, so that the true intensity of the humidity signals realized in the model is not necessarily weaker than that in other models.

It is notable in Fig. 26 that some amount of positive moisture anomalies exist at the precipitation maxima even in the models with weak signals in AD component. One would have a question why moisture in these models could not serve as a memory variable. It is the temperature field (Fig. 25) that gives us a clue to the question. As mentioned in section 5, there are distinct low temperature anomalies in the low levels of the atmosphere at around the precipitation maxima in the models with weak signals of AD component, i.e., in CSIRO, EC07, GSFC, and NCAR (Fig. 25(b),(d),(e) and (g)), whereas no low temperature anomaly exists in the low levels in AGUforAPE and ECMWF05 (Fig. 25(a) and (c)). The development of the low level cold temperature anomalies, which results from evaporation of raindrops, terminates the life of convective clouds (Nakajima and Matsuno 1988). Owing to the low level cold anomalies, grid scale convections in AGCMs, i.e., the updrafts of disturbances in AD component, shall also be prevented from having a long life time. From this viewpoint, however, the existence of low level cold anomaly in LASG (Fig. 25(f)) is troublesome. There should be some reason that suppresses the destructive effect of low level cold anomaly to have a significant amount of signals in AD component of LASG. This might be explained by the fact that latent heating in LASG extends to considerably lower levels (Fig. 27(f)) compared with those in the other models. Sensitivity of the behavior of grid scale convection to rain evaporation is also demonstrated by the contrast between the behaviors of AD component in ECMWF05 and ECMWF07; from the former to the latter, parameterization of rain evaporation is revised so as to increase the efficiency of rain evaporation (Bechtold et al. 2008), and intensity of disturbances in AD component decreases greatly [1] .

Finally, a remark is made on the effect of rain evaporation on the temperature and moisture signals. One may think that rain evaporation should increase moisture content at the place it occurs. Then, low level moisture should increase in the models with stronger rain evaporation. However, this is not true. In the models with active rain evaporation, such as GSFC and NCAR, there appear cold temperature and negative humidity anomalies in the low levels of the atmosphere (Fig. 26(e) and (g)). One should recognize that the evaporation of rain cools the atmosphere and induces downward motion, which contributes to drying the atmosphere.

[1] It is interesting to note that, the revision to enhance the rain evaporation not only suppress the grid scale convection of AD component but also enhance the disturbances of K component, although the reason remains unclear.

6.2 Comparison with observed Convectively Coupled Equatorial Waves

It would be desired to compare the behaviors of disturbances in the APE runs with CCEWs in the real atmosphere. However, we should be cautious in such comparison for at least two reasons. First, the behaviors of disturbances in the real atmosphere should be greatly affected by non-uniformity or asymmetry of the surface boundary conditions, which is one of the great differences between the APE and the real atmosphere. Second, quantities observed in the real atmosphere do not necessarily have temporal and/or spatial coverage, resolution, and uniformity. We have to keep in mind that attempts of comparison, which follows, inevitably remain superficial.

We should also note that wavenumber-frequency spectra of OLR, rather than precipitation in the present study, has been examined by a number of studies on CCEWs including Takayabu (1994a) and Wheeler and Kiladis (1999). However, Cho *et al.* (2004) examines the precipitation data from TRMM, and shows that the types and their characteristics of CCEWs found in TRMM data is consistent with those in OLR data. In the followings, we ignore the difference of keys between OLR and precipitation, unless special attention is necessary.

As reported in Wheeler and Kiladis (1999), the activity of CCEWs has a strong seasonal dependence. For the annual average of equatorially symmetric component, Fig.3(b) of Wheeler and Kiladis (1999) shows that signals of the Kelvin wave type are strong, while signals of the westward inertio gravity wave type are weak. The dominant wavenumber of the westward inertio gravity wave type is larger than four. In addition to those, signals of TD-type and also of the Rossby wave type exist, although dominant wavenumber for the Rossby wave type is smaller than the cutoff wavenumber of the filters used in the analyses of the present paper. As for the seasonal dependence, Fig.5(b) and (d) of Wheeler and Kiladis (1999) indicate that TD-type signals are much stronger in the northern summer, whereas signals of the other types are stronger in the southern summer. The dominant wavenumber of the signals of the westward inertio gravity wave type is from two to seven in the southern summer, and larger than seven in the northern summer. Now, the meridional distribution of CONTROL SST is relatively close to that of the southern summer than northern summer, we would expect strong signals for K and WIG components but weak signals for AD component in the results of the APE runs, if AD component could be regarded as the correspondence of TD-type. Actually, as was described in Section 4, most of the APE models are to some extent successful in producing abundant signals of K component. On the other hand signals of WIG component appear clearly only in a limited models in the APE; those are ECMWF05, LASG, and GSFC among the seven models that are intensively analyzed in this paper, and FRCGC and K1JAPAN among those not intensively analyzed. As described so far, the reason for the variety of representations of WIG component among the APE models, and hence the reason for difference from the observational characteristics are unclear.

Most of the APE models produce abundant signals of AD component. One might think that this contradicts the expectation above. But, one should remind that AD component in the APE runs differs from TD-type in Wheeler and Kiladis (1999) based on the following points. First, precipitations at the off-equatorial latitudes in the APE runs are weak (Fig.4 in Blackburn et al,2012a) because of the sharp peak of CONTROL SST (Fig. 1). Off-equatorial precipitation is one of the necessary ingredient of "TD" in the real atmosphere (Takayabu and Nitta, 1993). One cannot expect strong appearance of TD-type disturbances in the APE runs with CONTROL SST. Second, the key variable we chose to make the composite structures of AD component is precipitation at the equator. In the analyses presented in this paper, we focused on the disturbances associated with precipitation events close to the equator. Off-equatorial signals that may be corresponds to those of TD-type would be smeared out. In fact, the composite precipitation distributions at the off-equatorial latitudes of AD component are weak in all of the models (Fig. 22). Considering these points, AD component in this study should not be regarded as the correspondence of TD-type, but should be related to "background" component, which previous studies on CCEWs such as Wheeler and Kiladis (1999) have not concerned yet.

The spatial structures of CCEWs have been a subject of a number of investigations, such as Wheeler *et al.* (2000), Yang *et al.* (2007a, 2007b, 2007c) and other studies reviewed by Kiladis *et al.* (2009). It has been established that the vertical structure of temperature anomalies associated with the signals of the Kelvin wave type and the westward inertio gravity wave type is "boomerang" like (Fig.7 in Wheeler and Kiladis (1999) for the Kelvin wave type, and Fig.23 for the westward inertio gravity wave type), which can be interpreted as the internal waves emitted upward and downward from the strong convective heating whose maximum is located in the upper troposphere (e.g., Nitta and Esbensen, (1974); Houze, (1982); Takayabu *et al.*, (2010)) The longitudinal contrast of humidity in the lower troposphere around the precipitation peak, i.e., more humid before convection and drier after, is another important feature. Those structures are reproduced in only a small number of models in the APE analyzed here; ECMWF05, ECMWF07 and LASG are good for K component, and only LASG is good for WIG component. The performance of FRCGC in representing disturbances of the Kelvin wave type seems to be quite successful, as is extensively described in Nasuno *et al.* (2008), but that for the westward inertio gravity wave type is not known.

As for the horizontal structures of CCEWs in the real atmosphere, those for the Kelvin and Rossby wave types are extracted and investigated by Yang *et al.* (2007c), where the difference of the structures between the eastern and western hemispheres are considered. Kiladis *et al.* (2009) confirm the major features of the composite structures by Yang *et al.* (2007c). Consulting Fig.1 of Yang *et al.* (2007c), we can find that the structures for K components in the APE runs examined here are closer to that in the western hemisphere, considering the presence of significant meridional wind perturbation in the lower troposphere and considerable rotational wind component in the upper troposphere. Either of the structure of the Rossby wave type for the western or the eastern hemisphere (Fig.5 and Fig.9 of Yang *et al.*, 2007c, respectively) is not similar to those for AD components in most of the APE models presented here, since the structure of the Rossby wave type contains a pair of distinct off-equatorial vortical cells in the lower troposphere. As is noted earlier, the off-equatorlai low level rotational signals can be identified only in a small number of models (AGUforAPE and CSIRO). And even in these models, the locations of the maxima of vorticities are much closer to the equator compared with those in Yang *et al.* (2007c). Finally, the horizontal structure for the westward inertio gravity wave type is presented in Kiladis *et al.* (2009). Generally the structures for WIG components in the APE runs examined here are close to that of Kiladis *et al.* (2009).

Considering the difference between the definition of the Rossby wave type in those papers and that of AD component in this paper, the difference between the properties for the Rossby wave type and those for AD component is trivial. As for the Rossby wave type, additional data analysis focusing more sharply on the region of wavenumber frequency domain of the Rossby wave type is required, which is left for a future study. The effect on the appearances and the structures of CCEWs caused by the difference of the meridional profile of SST in the real world and the CONTROL profile of the APE is an interesting issue. It would be useful to compare the appearances and the structures of CCEWs that appear in the APE experiments but with the SST profiles other than CONTROL. However, this is also left for a future study, because complete re-run of the models for those SST profiles are indispensable in order to collect the necessary data.

It is interesting to note that LASG, which is equipped with the simplest cumulus parameterization scheme among the APE models, i.e., convective adjustment of Manabe *et al.* (1965), shows rather good performance in the representation of signals of WIG component in the wavenumber-frequency spectrum. It is better than the other intensely considered models in this paper, which are equipped with various kind of more complex cumulus schemes in several aspects, and is probably comparable to FRCGC consulting the distribution of signals which extend around the westward inertio gravity wave modes shown in Fig. 4(h). Most of the APE models are tuned to reproduce climatological states of the atmosphere. And hence it is understandable that the disturbances of WIG component, which have short periods and their relationship to the long-time and/or large-scale atmospheric states is not direct, have not been a subject of extensive tuning. This situation might have changed a lot since the execution of the APE, and models of more recent generation may present much better performance.

6.3 Comparison with Convectively Coupled Equatorial Waves represented in previous modeling studies

Disturbances of the Kelvin wave type have been investigated in several modeling studies including those with the aqua-planet setup (e.g., Frierson, 2007; Lee *et al.*, 2003) or those with realistic surface boundary condition (e.g., Lee *et al.*, 2003; Suzuki *et al.*,2006; Frierson *et al.*, 2010). The aim of these studies is to investigate the responses of the representation of the Kelvin wave type disturbances to the changes of the processes or the parameters implemented in a model, and to improve the representation of the Kelvin wave type in the model. The structures of the Kelvin wave type presented in those studies, if successfully represented in the Hovmëllor plot or wavenumber-frequency, share several aspects with observed disturbances of the Kelvin wave type such as the "boomerang" like vertical structure of temperature. Compared with the similarity among the structures of those successful cases, the structures of K component in the APE runs described in this paper exhibit quite wider variety. Intercomparison study of the disturbances of the Kelvin wave type somewhat similar to the present study has been done in CMIP3 (Coupled Model Intercomparison Project phase 3) by Straub *et al.* (2010). Although the comparison of the structures is, as in the present paper, limited to a small number of models, considerable diversity is found both in the horizontal and in the vertical structures, again as in the present paper. All of these past and present results suggest that there is much room for improvement of the representation of the disturbances of the Kelvin wave type.

So long as we know, disturbances of the westward inertio gravity wave type and disturbances of the advective component in GCMs. have not been investigated intensely, although there are studies on disturbances of the Rossby wave type (e.g., Suzuki *et al.*, 2006; Yang *et al.*, 2009) and those of TD-type in GCMs.

6.4 Other branches in the wavenumber-frequency space

With different specification of the SST profile, the space time structure of equatorial precipitation varies as described in Blackburn *et al.* (2012b). Still, most of the signals in wavenumber-frequency spectra can be classified as Kelvin, WIG and AD components. However, relative power among the three types of signals varies reflecting the change of space time structure of precipitation responding to the change of SST profile. Here we mention only two of the notable features observed in the runs with the SST profile other than CONTROL, i.e., FLAT.

In FLAT experiment of ECMWF07, not only westward but but also eastward inertio gravity wave signals appear distinctly. This may be understandable by considering that the latitudinal width of the equatorial precipitation region is much broader with the FLAT SST profile than with the CONTROL SST; n=1 eastward inertio gravity wave mode, which has a latitudinally more extended region of convergence than corresponding n=1 westward wave mode, can interact with moist convection more easily. Actually, signals of the eastward inertio gravity wave type can be found in the symmetric component of wavenumber-frequency spectrum of precipitation in the latitudinal band of 10-20 degree (not shown). That is the latitude of the off-equatorial peaks of convergence for n=1 eastward inertio gravity wave mode, for example, see Fig.3 of Yang *et al.* (2003). However, the reason is unclear why signals of the eastward inertio gravity wave type do not appear in the FLAT experiment with the models other than ECMWF07 despite that most of them are also characterized with broad ITCZ.

We mentioned earlier the possible existence of disturbances of the eastward inertio gravity wave type also in CONTROL of NCAR. We did not perform detailed analysis on the off equatorial structure, so that no firm conclusion is admitted presently. It may worth pointing out, however, that the appearance of disturbances of the eastward inertio gravity wave type in CONTROL of NCAR is consistent with that in FLAT of ECMWF07. They are the cases with double ITCZ or broad ITCZ, which permit the coupling between convective heating and wave motion not only at the equator but also in the off-equatorial latitudes. Still, actual emergence of the coupling is not simple, because, despite the fact that the ITCZs are broad or double in some runs other than CTCL of NCAR and FLAT of ECMWF07, disturbances of the eastward inertio gravity wave type can not be identified in those runs. In order to investigate these issues, further investigation is necessary with complete datasets provided by re-run of models.

6.5 Relationship between the height of convective heating and phase speed of disturbances

The vertical structures of convective heating for the three spectral filtered components are slightly different (Fig. 13, Fig. 20, Fig. 27) for all models. If we compare them carefully, we can notice that, in all of the models, the weighted centers of convective heating are located at the lower altitudes for WIG, at the heigher altitudes for AD, and in between for K. Interestingly, the above order follows the reverse of the magnitude of phase velocity of the disturbances relative to the low level zonal wind. In other words, if this is true, the altitude of the center of convective heating decreases as the increase of the magnitude of intrinsic phase velocity. This tendency of heating profile might be understandable if one recalls that the development of parameterized moist convection requires a certain degree of moisture accumulation, for which a certain length of time would be necessary. If the intrinsic frequency of a disturbance be shorter than its moisture accumulation time scale, convective heating might be unable to respond. The sensitivity of heating to the period of disturbance is similar to, but slightly different from, the idea of "phase lagged wave-CISK" proposed by Davies (1979), or "convective response time" discussed by several authors (e.g. Emanuel, 1993; Emanuel *et al.*, 1994; Lindzen, 2003). In phase-lagged wave-CISK, phase difference between the longitudinal positions of heating and low level upward motion is assumed to depend on the wave period. In the effect of convective response time formulated by Emanuel (1993), the intensity of heating is assumed to depend on the wave period. In the results of the present study, there is a possibility that the vertical structures of heating depend on the characteristic period of disturbances. This is an interesting possibility which could lead to another way of eliminating the “ultraviolet catastrophe” from the classical wave-CISK theory. However, before going further, existence and structure of the dependence of heating on the intrinsic period of disturbances in GCMs should be investigated more carefully. Interaction between convection and circulation is a difficult issue in general, and is even more intricate under the performance of a cumulus parameterization scheme. The issue is left for future research.

7. Concluding remarks

We have examined the APE results focusing mainly on the structures associated with equatorial precipitation activities in the subset of the APE participating models on which detailed time series of the model variables are available. The summary of results are presented in abstract so is not to be repeated here.

We should mention that the simple and idealized setup of the APE project has been quite successful in elucidating the similarities and differences of the equatorial precipitation structures in different models. However, it is still quite difficult to explain what kind of differences in the choice of implementation of physical processes are related to particular differences of the composite structures. The source of difficulty is at least three-fold. First, the different cumulus parameterizations contain different sets of internal variables and the output variables. Meaningful comparison among the behaviors of parameterizations is not a easy task. Second, partly due to the difficulty noted above, we could not define appropriate datasets to describe the behaviors of implementations of physical processes before the call of the APE project. We could not obtain consistent datasets from the participating groups. Third, as is almost always applicable to analysis of atmospheric models, complex entangled interplay among various dynamical and physical processes in the models makes clear, simple interpretation difficult in spite of the simple and unified external setup of the APE.

We can not be sure on to what extent the results of the present study can be applied to the behavior of precipitation features in more realistic setup. This is partly because we analyze only the subset of CONTROL runs, which is, in itself, a subset of the specifications of the APE. It should be bear in mind that the CONTROL case may not be most representative setup among the cases defined in the APE. For example, as described in Blackburn *et al.* (2011a) and the APE-ATLAS (Williamson et al. 2011), ITCZ precipitation is too much concentrated at the equator and zonal mean zonal wind of the upper troposphere around the equator is rather intense westerly in most models. The former point may affect on many aspects of properties of convectively coupled equatorial disturbances, and the latter point may affect the intensity and characteristics of the interaction between the tropics and the mid-latitudes. It is clear that the present analysis should be supplemented by analyses of other cases, i.e., FLAT, QOBS and PEAKED. However, regrettably, the composite analysis of those cases requires time series of three dimensional model variables and tendency data that were not submitted on the most of the participating models.

Lastly, we comment on the necessity of "APE2", i.e., another execution of aqua-planet experiment project. The numerical experiments for the present APE by the participating groups were conducted in the period of 2002–2007. Some of the results of this study, namely the large degree of diversity found in the properties of precipitation such as the intensities of signals for K, WIG, and AD components and the vertical structures of the composites for those three may originate from immaturity of the atmospheric models in that period. The same can be claimed about other diversity found among the different models described in APE-ATLAS and Blackburn *et al.* (2011a, b). Because global atmospheric models have been developing extensively in many aspects such as spatial resolution and various processes of physics, it is worth repeating the APE in a basically the same framework. It is particularly interesting to examine whether the current generation of atmospheric models will still exhibit diversity like shown in this paper or not. In the possible repetition of the APE, it should be important to collect more complete datasets on all of the cases; the time series of the lower levels of the atmosphere are indispensable to examine the tropical disturbances. Finally, it should be stressed that, not only to compare but also to interpret the results of experiments, thorough description of numerical models is indispensable. It would be ideal that every participating group would provide the source code of the numerical model used and interested members can re-run models of other groups. Such a deep level of collaboration may not be established very easily, but will be very fruitful for the advancement of modeling community.

Appendix

As mentioned in section 5.2.a, the composite structure of K component is associated with significant off-equatorial rotational signature. In Fig. 10, however, neither the latitudinal extent nor the structure of the rotational signature is evident. In this appendix, the upper tropospheric rotational features in the subtropical and extratropical latitudes are more explicitly presented in terms of stream function. The method of analysis is as follows:

(i) relative vorticity is calculated from the horizontal wind of the composite data for K component for each model, (ii) stream function is obtained from the relative vorticity field through the inversion of spherical Laplacian operator employing the spectral method.

Figure 29 show the stream function field. Since the structures are nearly antisymmetric about the equator, only those of the northern latitudes are plotted. Distinct rotational component is found in all models. For most of the models, the structure of stream function consists of a train of vortices with alternating signature along the latitudes of $\sim 25°$; anticyclone is located at about the longitude of the precipitation maximum.

These vortical features resemble to some extent that obtained by Yang *et al.* (2007a, b, c), where disturbances of the n=1 Rossby wave type propagating eastward because of Doppler shift by the zonal mean westerly wind are identified. However, we hesitate to identify the structure shown in Figure 29 as that obtained by Yang *et al.* (2007a, b, c) based on the following concerns. First, the peaks of the rotational structures of stream functions obtained here are located at much higher latitudes compared with that of n=1 Rossby mode of Yang *et al.* (2007a, b), although the difference could be resulting from the difference magnitude of the ambient potential vorticity gradient in the cases examined by Yang *et al.* (2007a, b,c) and that in the CONTROL expeiments of the APE. Second, the n=1 Rossby mode of Yang *et al.* (2007b, c) are found to be excited mainly by the convection located off-equatorial latitudes around $\sim 10^\circ$, where the precipitation is quite weak in CONTROL experiments in all of the models in the APE (Blackburn et al. 2012a). The disturbances of the APE runs have the features of mid-latitude Rossby waves trapped within the strong westerly jets of the APE runs rather than the features of equatorial Rossby waves.

The existence of these vortical signatures and their commonality among the different APE models suggest an existence of dynamical connection between subtropical vortical anomalies and equatorial precipitation, i.e., equatorial precipitation can force subtropical vortices, or vice versa. A key factor that allows such connection between equatorial convection and subtropical and/or mid-latitude vorticity is the zonal mean westerly wind covering all latitudes in the upper troposphere. The emergence strong westerly jet is one of the unique features of the CONTROL experiment of the APE (see Blackburn *et al.*, 2011a). However, further investigation of underlying physics is left for future research. Fig. 29

Acknowledgements

The authors thank the APE participants, especially those of CSIRO, ECMWF, GSFC, LASG, and, NCAR for providing the additional transient data used in this study. The authors also thank anonymous reviewers for reading this heavy manuscript and providing many constructive comments. Stimulative and encouraging discussions with Drs. M. Blackburn and D. L. Williamson were the great pabulum to accomplish this work. Numerical integrations of AGUforAPE were performed at the Earth Simulator Center. Analysis software and local computational environments were constructed by the use of the resources of GFD-DENNOU-CLUB, including GPhys, spmodel, and DCL and by the instructions from Drs S. Takehiro and Y. Sasaki of Kyoto University. This work was supported by Grants-in-Aid(B) for Scientific Research (12440123 and 21340139) of Japan Society for the Promotion of Science.

References

Andersen, J. A., and Z. Kuang, 2008: A toy model of the instability in the equatorially trapped convectively coupled waves on the equatorial beta plane. *J. Atmos. Sci*, **65**, 3736–3757.

Arakawa, A., and W. H. Schubert, 1974: Interaction of a cumulus cloud ensemble with the large-scale environment, part I. *J. Atmos. Sci*, **31**, 674–701.

Bechtold, P., M. Köhler, T. Jung, F. Doblas-Reyes, M. Leutbecher, M. J. Rodwell, F. Vitart, and G. Balsamo, 2008: Advances in simulating atmospheric variability with the ecmwf model: From synoptic to decadal time-scales. *Q. J. R. Meteorol. Soc.*, **134**, 1337–1351.

Blackburn, M., and B. J. Hoskions, 2012: Context and aims of the aqua planet experiment. *J. Meteor. Soc. Japan*, **APE Special Issue**, submitted.

Blackburn, M., D. L. Williamson, K. Nakajima, W. Ohfuchi, Y. O. Takahashi, Y.-Y. Hayashi, H. Nakamura, M. Ishiwatari, J. McGregor, H. Borth, V. Wirth, H. Frank, P. Bechtold, N. P. Wedi, H. Tomita, M. Satoh, M. Zhao, I. M. Held, M. J. Suarez, M.-I. Lee, M. Watanabe, M. Kimoto, Y. Liu, Z. Wang, A. Molod, K. Rajendran, A. Kitoh, and R. Stratton, 2012a: The aqua planet experiment (APE): CONTROL SST simulation. *J. Meteor. Soc. Japan*, **APE Special Issue**, submitted.

Blackburn, M., D. L. Williamson, K. Nakajima, W. Ohfuchi, Y. O. Takahashi, Y.-Y. Hayashi, H. Nakamura, M. Ishiwatari, J. McGregor, H. Borth, V. Wirth, H. Frank, P. Bechtold, N. P. Wedi, H. Tomita, M. Satoh, M. Zhao, I. M. Held, M. J. Suarez, M.-I. Lee, M. Watanabe, M. Kimoto, Y. Liu, Z. Wang, A. Molod, K. Rajendran, A. Kitoh, and R. Stratton, 2012b: The aqua planet experiment (APE):

Response to changed meridional SST profile. *J. Meteor. Soc. Japan*, **APE Special Issue**, submitted.

Chang, C. P., and H. Lim, 1988: Kelvin wave-cisk: A possible mechanism for the 30-50 day oscillations. *J. Atmos. Sci*, **45**, 1709–1720.

Cho, H. K., K. P. Bowman, and G. R. North, 2004: Equatorial waves including the madden-julian oscillation in trmm rainfall and olr data. *J. Climate*, **17**, 4387–4406.

Davies, H. C., 1979: Phase-lagged wave-cisk. *Q. J. R. Meteorol. Soc.*, **105**, 325–353.

Emanuel, K. A., 1987: An air-sea interaction model of intraseasonal oscillations in the tropics. *J. Atmos. Sci*, **44**, 2324–2340.

Emanuel, K. A., 1993: The effect of convective response time on wishe modes. *J. Atmos. Sci*, **50**, 1763–1763.

Emanuel, K. A., D. J. Neelin, and C. S. Bretherton, 1994: On large-scale circulations in convecting atmospheres. *Q. J. R. Meteorol. Soc.*, **120**, 1111–1143.

Frierson, D., D. Kim, I.-S. Kang, M.-I. Lee, and J. Lin, 2010: Structure of AGCM-simulated convectively coupled kelvin waves and sensitivity to convective parameterization. *J. Atmos. Sci*, **68**, 26–45.

Frierson, D. M. W., 2007: Convectively coupled kelvin waves in an idealized moist general circulation model. *J. Atmos. Sci*, **64**, 2076–2090.

Gill, A. E., 1982: Studies of moisture effects in simple atmospheric models: The stable case. *Geophys. Astrophys. Fluid Dyn.*, **19**, 119–152.

Haertel, P. T., and G. N. Kiladis, 2004: Dynamics of 2-day equatorial waves. *J. Atmos. Sci*, **61**, 2707–2721.

Hayashi, Y., 1970: A theory of large-scale equatorial waves generated by condensation heat and accelerating the zonal wind. *J. Meteor. Soc. Japan*, **48**, 140–160.

Hayashi, Y.-Y., and A. Sumi, 1986: The 30-40 day oscillations simulated in an "aqua planet" model. *J. Meteor. Soc. Japan*, **64**, 451–467.

Hendon, H. H., and M. C. Wheeler, 2008: Some space-time spectral analyses of tropical convection and planetary-scale waves. *J. Atmos. Sci*, **65**, 2936.

Houze, Jr, R. A., 1982: Cloud clusters and large-scale vertical motions in the tropics. *J. Meteor. Soc. Japan*, **60**, 396–410.

Houze, Jr, R. A., and A. K. Betts, 1981: Convection in gate. *Rev. Geophys.*, **19**, 541–576.

Kiladis, G. N., M. C. Wheeler, P. T. Haertel, K. H. Straub, and P. E. Roundy, 2009: Convectively coupled equatorial waves. *Rev. Geophys.*, **47**.

Kuang, Z., 2008: A moisture-stratiform instability for convectively coupled waves. *J. Atmos. Sci*, **65**, 834–854.

Kuang, Z., 2010: Linear response function of a cumulus ensemble to temperature and moisture perturbations and implications for the dunamics of convectively coupled waves. *J. Atmos. Sci*, **67**, 941–962.

Kuang, Z., P. N. Blossey, and C. S. Bretherton, 2005: A new approach for 3d cloud-resolving simulations of large-scale atmospheric circulation. *Geophys. Res. Lett.*, **32(L02809)**, 1–4.

Lau, K. M., and L. Peng, 1987: Origin of low-frequency (intraseasonal) oscillations in the tropical atmosphere. part I: Basic theory. *J. Atmos. Sci*, **44**, 950–972.

Lee, M. I., I. S. Kang, and B. E. Mapes, 2003: Impacts of cumulus convection parameterization on aqua-planet AGCM simulations of tropical intraseasonal variability. *J. Meteor. Soc. Japan*, **81**, 963–992.

Lindzen, R. S., 2003: The interaction of waves and convection in the tropics. *J. Atmos. Sci*, **60**, 3009–3020.

Madden, R. A., and P. R. Julian, 1972: Description of global-scale circulation cells in the tropics with a 40–50 day period. *J. Atmos. Sci*, **29**, 1109–1123.

Madden, R. A., and P. R. Julian, 1994: Observations of the 40-50-day tropical oscillation-a review. *Mon Wea. Rev.*, **122**, 814–837.

Manabe, S., J. Smagorinsky, and R. F. Strickler, 1965: Simulated climatology of a general circulation model with a hydrologic cycle 1. *Mon Wea. Rev.*, **93**, 769–798.

Mapes, B., S. Tulich, J. Lin, and P. Zuidema, 2006: The mesoscale convection life cycle: Building block or prototype for large-scale tropical waves? *Dyn. Atmos. Ocean*, **42**, 3–29.

Matsuno, T., 1966: Quasi-geostrophic motions in the equatorial area. *J. Meteor. Soc. Japan*, **44**, 25–42.

Matthews, A. J., and R. A. Madden, 2000: Observed propagation and structure of the 33-h atmospheric kelvin wave. *J. Atmos. Sci*, **57**, 3488–3497.

Miura, H., H. Tomita, T. Nasuno, S. Iga, M. Satoh, and T. Matsuno, 2005: A climate sensitivity test using a global cloud resolving model under an aqua planet condition. *Geophys. Res. Lett.*, **32**, L19717.

Nakajima, K., and T. Matsuno, 1988: Numerical experiments concerning the origin of cloud clusters in the tropical atmosphere. *J. Meteor. Soc. Japan*, **66**, 309–329.

Nakajima, K., Y. Yamada, M. Ishiwatari, and Y.-Y. Hayashi, 2012: Dependence of equatorial precipitation activity on the vertical profile of radiative cooling in an aqua-planet experiment. *Nagare*, **31 (Nagare Multimedia 2012)**, http://www2.nagare.or.jp/mm/2012/nakajima/index.htm.

Nakajima, K., Y. Yamada, Y. Takahashi, M. Ishiwatari, W. Ohfuchi, and Y.-Y. Hayashi, 2011: The variety of forced atmospheric structure in response to tropical SST anomaly found in APE results. *J. Meteor. Soc. Japan*, **APE Special Issue**, submitted.

Nasuno, T., H. Tomita, S. Iga, H. Miura, and M. Satoh, 2008: Convectively coupled equatorial waves simulated on an aquaplanet in a global nonhydrostatic experiment. *J. Atmos. Sci*, **65**, 1246–1265.

Neale, R. B., and B. J. Hoskins, 2000: A standard test for AGCMs including their physical parametrizations: I: The proposal. *Atmos. Sci. Lett.*, **1**, 101–107.

Neelin, D. J., I. M. Held, and K. H. Cook, 1987: Evaporation-wind feedback and low-frequency variability in the tropical atmosphere. *J. Atmos. Sci*, **44**, 2341–2348.

Nitta, T., and S. Esbensen, 1974: Heat and moisture budget analyses using momex data. *Mon Wea. Rev.*, **102**, 12–28.

Numaguti, A., and Y.-Y. Hayashi, 1991a: Behavior of cumulus activity and the structures of circulations in an" aqua planet" model part I: The structure of the super clusters. *J. Meteor. Soc. Japan*, **69**, 541–561.

Numaguti, A., and Y.-Y. Hayashi, 1991b: Behavior of cumulus activity and the structures of circulations in an" aqua planet" model part II: Eastward-moving planetary scale structure and the intertropical convergence zone. *J. Meteor. Soc. Japan*, **69**, 563–579.

Sardeshmukh, P. D., and B. J. Hoskins, 1988: The generation of global rotational flow by steady idealized tropical divergence. *J. Atmos. Sci*, **45**, 1228–1251.

Satoh, M., T. Matsuno, H. Tomita, H. Miura, T. Nasuno, and S. Iga, 2008: Nonhydrostatic icosahedral atmospheric model (NICAM) for global cloud resolving simulations. *J. Comput. Phys.*, **227**, 3486–3514.

Sherwood, S. C., R. Roca, T. M. Weckwerth, and N. G. Andronova, 2010:

Tropospheric water vapor, convection, and climate. *Rev. Geophys.*, **48**, RG2001.

Straub, K. H., P. T. Haertel, and G. N. Kiladis, 2010: An analysis of convectively coupled kelvin waves in 20 WCRP CMIP3 global coupled climate models. *J. Climate*, **23**, 3031–3056.

Straus, D. M., and R. S. Lindzen, 2000: Planetary-scale baroclinic instability and the MJO. *J. Atmos. Sci*, **57**, 3609–3626.

Suzuki, T., Y. N. Takayabu, and S. Emori, 2006: Coupling mechanisms between equatorial waves and cumulus convection in an AGCM. *Dyn. Atmos. Ocean*, **42**, 81–106.

Takayabu, Y. N., 1994a: Large-scale cloud disturbances associated with equatorial waves. i: Spectral features of the cloud disturbances. *J. Meteor. Soc. Japan*, **72**, 433–449.

Takayabu, Y. N., 1994b: Large-scale cloud disturbances associated with equatorial waves. II: Westward-propagating inertio-gravity waves. *J. Meteor. Soc. Japan*, **72**, 451–465.

Takayabu, Y. N., and T. Nitta, 1993: 3-5 day-period disturbances coupled with convection over the tropical pacific ocean. *J. Meteor. Soc. Japan*, **71**, 221–246.

Takayabu, Y. N., S. Shige, W.-K. Tao, and N. Hirota, 2010: Shallow and deep latent heating modes over tropical oceans observed with trmm pr spectral latent heating data. *J. Climate*, **23**, 2030–2046.

Tao, W. K., and M. W. Moncrieff, 2009: Multiscale cloud system modeling. *Rev. Geophys.*, **47**, RG4002.

Tiedtke, M., 1989: A comprehensive mass flux scheme for cumulus parameterization in large-scale models. *Mon Wea. Rev.*, **117**, 1779–1800.

Wheeler, M., and G. N. Kiladis, 1999: Convectively coupled equatorial waves: Analysis of clouds and temperature in the wavenumber-frequency domain. *J. Atmos. Sci*, **56**, 374–399.

Wheeler, M., G. N. Kiladis, and P. J. Webster, 2000: Large-scale dynamical fields associated with convectively coupled equatorial waves. *J. Atmos. Sci*, **57**, 613–640.

Williamson, D. L., M. Blackburn, B. Hoskins, K. Nakajima, W. Ohfuchi, Y. O. Takahashi, Y.-Y. Hayashi, H. Nakamura, M. Ishiwatari, J. McGregor, H. Borth, V. Wirth, H. Frank, P. Bechtold, N. P. Wedi, H. Tomita, M. Satoh, M. Zhao, I. M. Held, M. J. Suarez, M.-I. Lee, M. Watanabe, M. Kimoto, Y. Liu, Z. Wang, A. Molod, K. Rajendran, K. A., and R. Stratton, 2011: *The APE Atlas. NCAR/TN-484+STR*. Natilnal Center for Atmospheric Research.

Woolnough, S. J., J. M. Slingo, and B. J. Hoskins, 2004: The diurnal cycle of convection and atmospheric tides in an aquaplanet GCM. *J. Atmos. Sci*, **61**, 2559–2573.

Yang, G. Y., B. Hoskins, and J. Slingo, 2003: Convectively coupled equatorial waves: A new methodology for identifying wave structures in observational data. *J. Atmos. Sci*, **60**, 1637–1654.

Yang, G. Y., B. Hoskins, and J. Slingo, 2007a: Convectively coupled equatorial waves. part 1: Horizontal and vertical structures. *J. Atmos. Sci*, **64**, 3406–3423.

Yang, G. Y., B. Hoskins, and J. Slingo, 2007b: Convectively coupled equatorial waves. part 2: Propagation characteristics. *J. Atmos. Sci*, **64**, 3424–3437.

Yang, G. Y., B. Hoskins, and J. Slingo, 2007c: Convectively coupled equatorial waves. part 3: Synthesis structures and their forcing and evolution. *J. Atmos. Sci*, **64**, 3438–3451.

Yang, G. Y., J. Slingo, and B. Hoskins, 2009: Convectively coupled equatorial waves in high-resolution hadley centre climate models. *J. Climate*, **22**, 1897–1919.

Zappa, G., V. Lucarini, and A. Navarra, 2011: Baroclinic stationary waves in aquaplanet models. *J. Atmos. Sci*, **68**, 1023–1040.

List of Figures

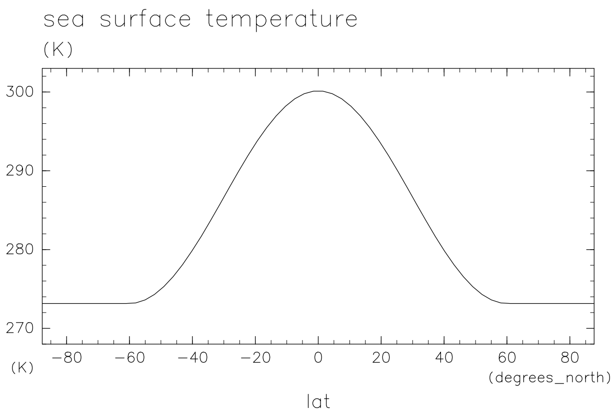

Fig. 1. Meridional distribution of sea surface temperature [K] in CONTROL experiment.

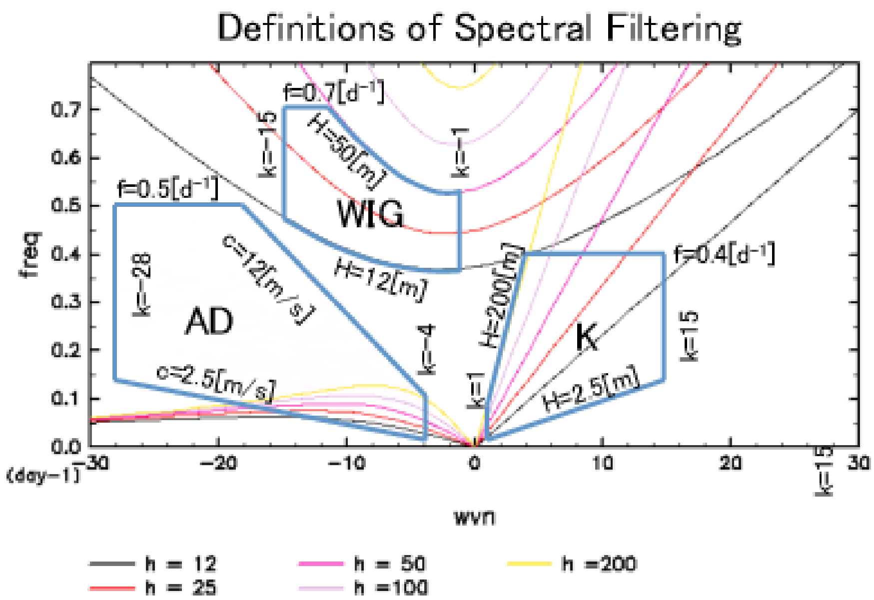

Fig. 2. Definition of spectral filters.

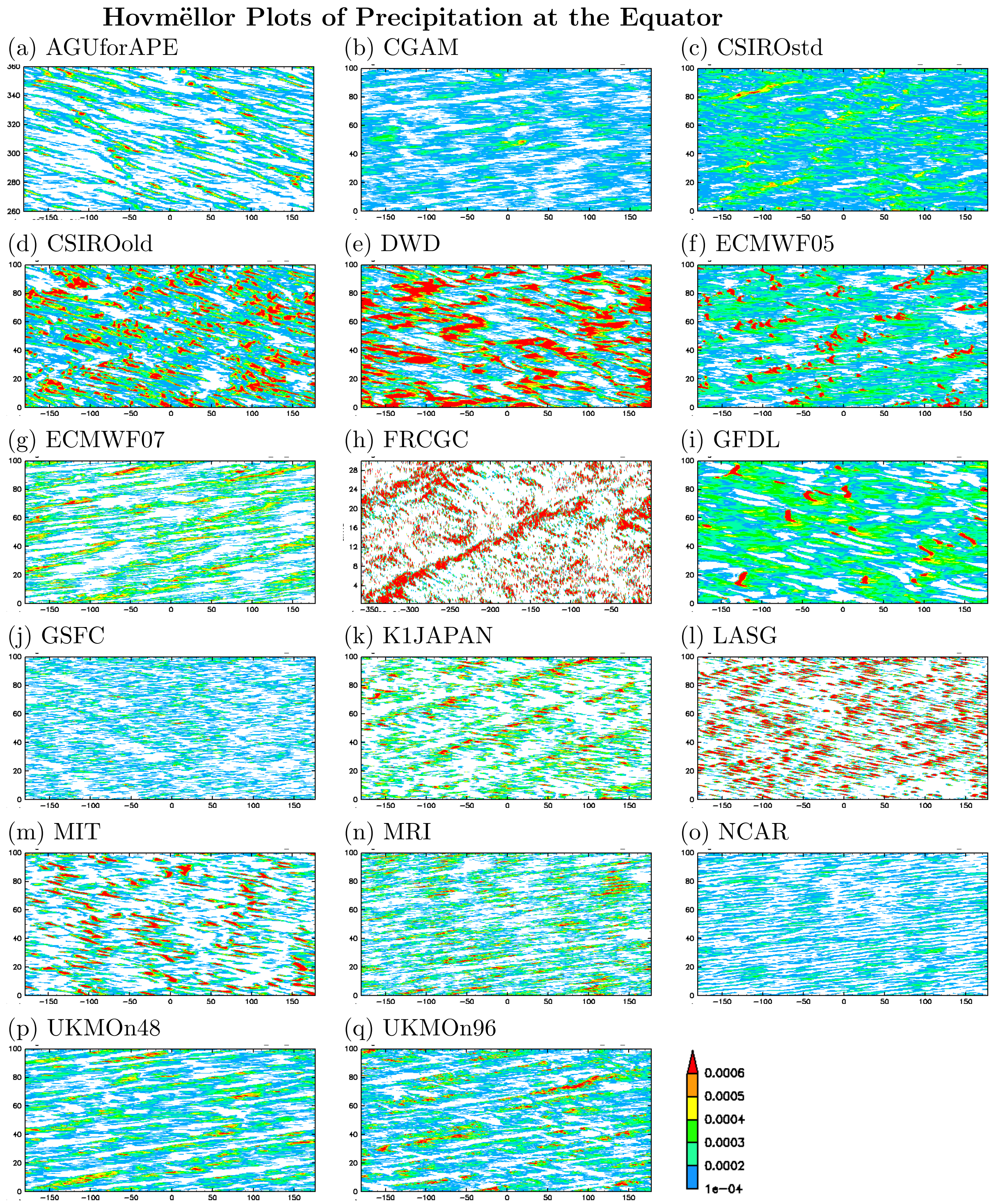

Fig. 3. Example Hovmëllor plots of equatorial precipitation of the APE runs for a duration of 100 days except for 30 days of (h) FRCGC. Horizontal axes represent longitude, and vertical axes represent time going up. Unit is kg m^{-2} s^{-1}.

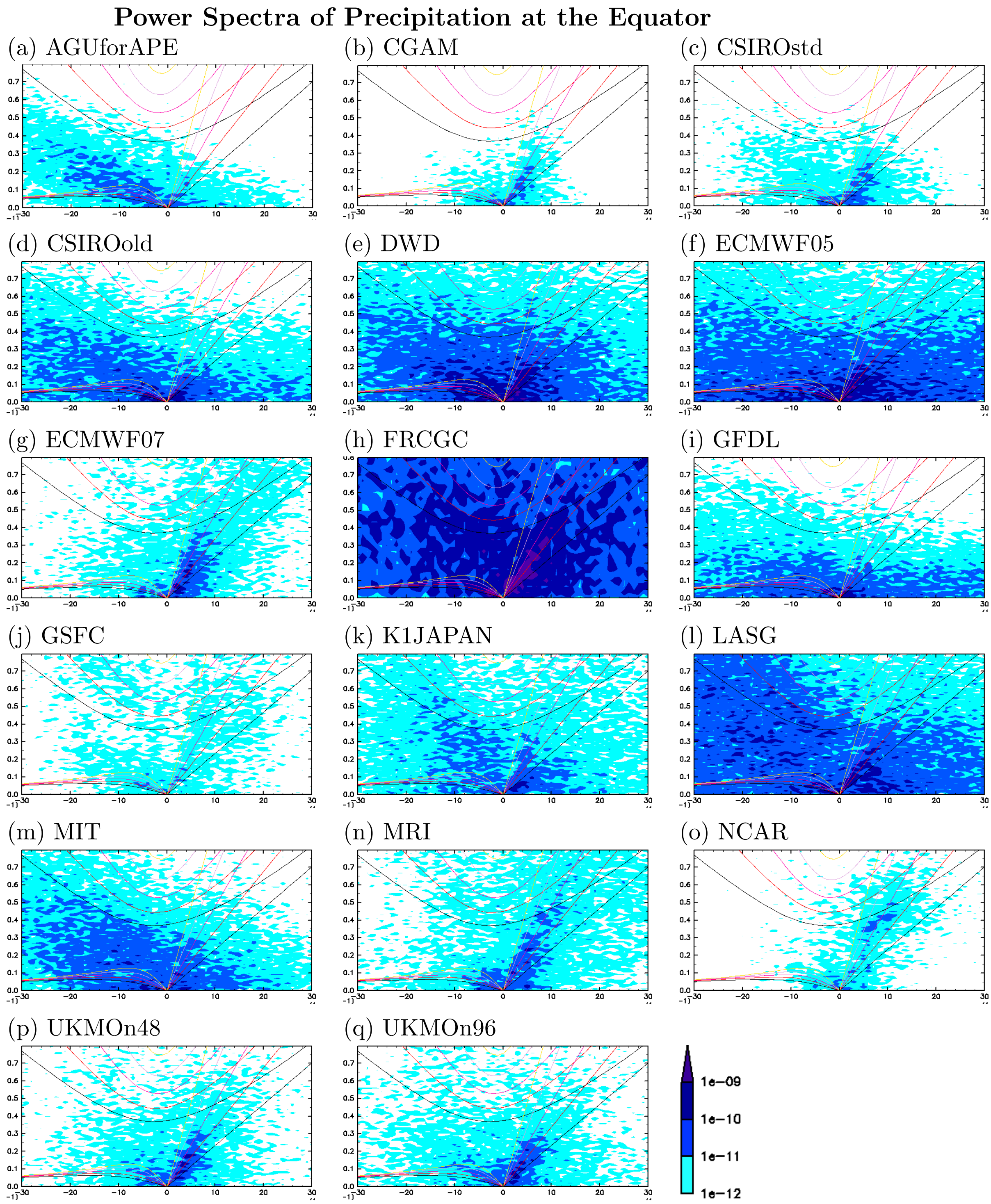

Fig. 4. Wavenumber-frequency spectra of precipitation at the equator. Unit is $kg^2\ m^{-4}\ s^{-2}$. Horizontal axes represent zonal wavenumber from -30 to 30, and vertical axes represent frequency from 0 to 0.8 [day^{-1}]. The positive (negative) zonal wavenumber represents eastward (westward) propagation.

Enhanced Power Spectra of Precipitation at the Equator

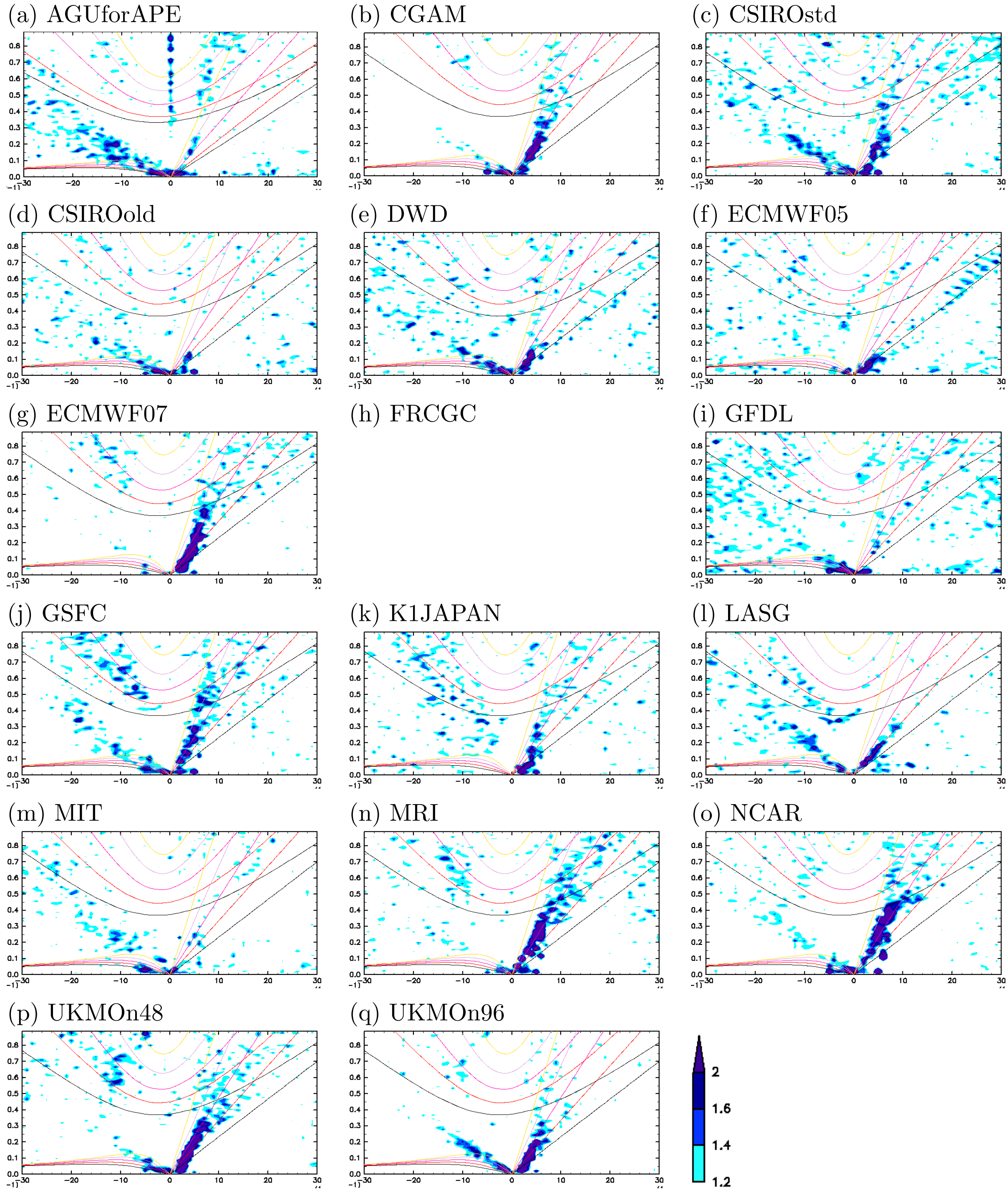

Fig. 5. Same as Fig.4 but for the intensity relative to the background level (Wheeler and Kiladis 1999, see text). The figure for FRCGC is not produced.

(a)

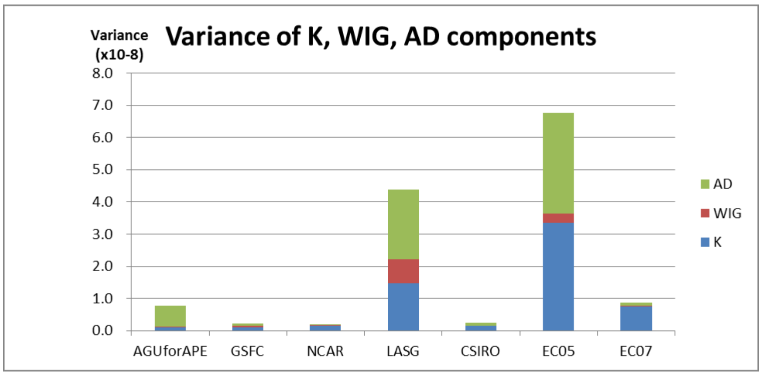

(b)

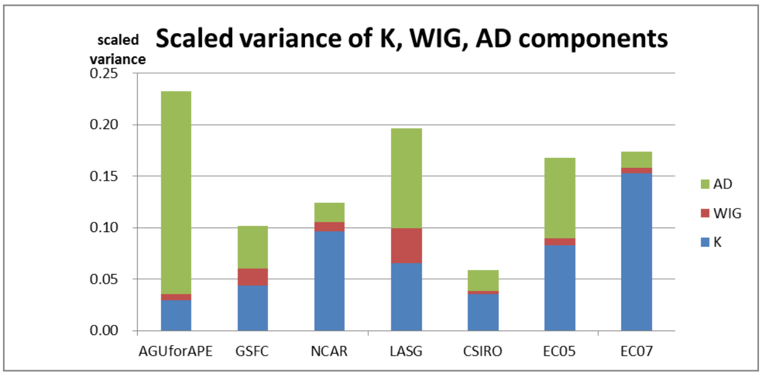

Fig. 6. (a) Variance of precipitation along equator for K, WIG, and AD components. Unit is $[(\mathrm{kg/m^2s})^2]$. (b) Same as (a), but for the values normalized by the total variance of precipitation.

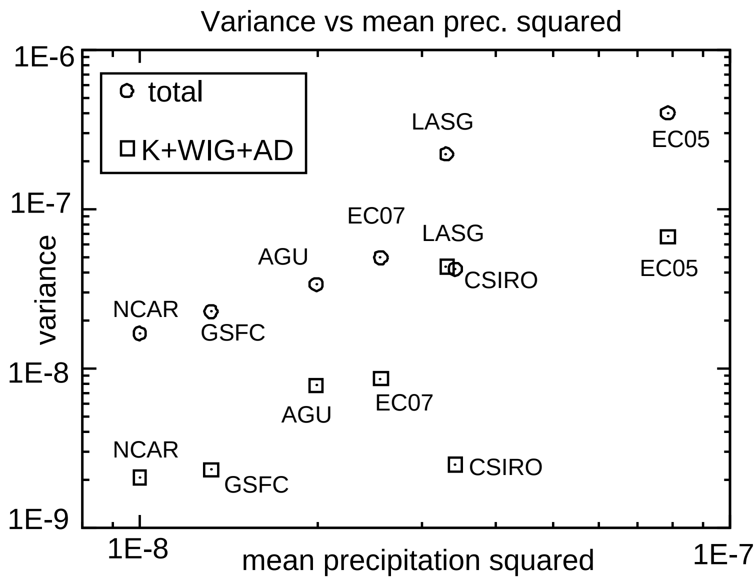

Fig. 7. Scattering diagram showing the relationship between the average precipitation squared and total variance of precipitation along the equator. Unit is $[(\mathrm{kg/m^2s})^2]$. Circles indicate the sum of the variance of K, WIG, AD components, and squares indicate the total variance.

K Composite: RAIN & uv925

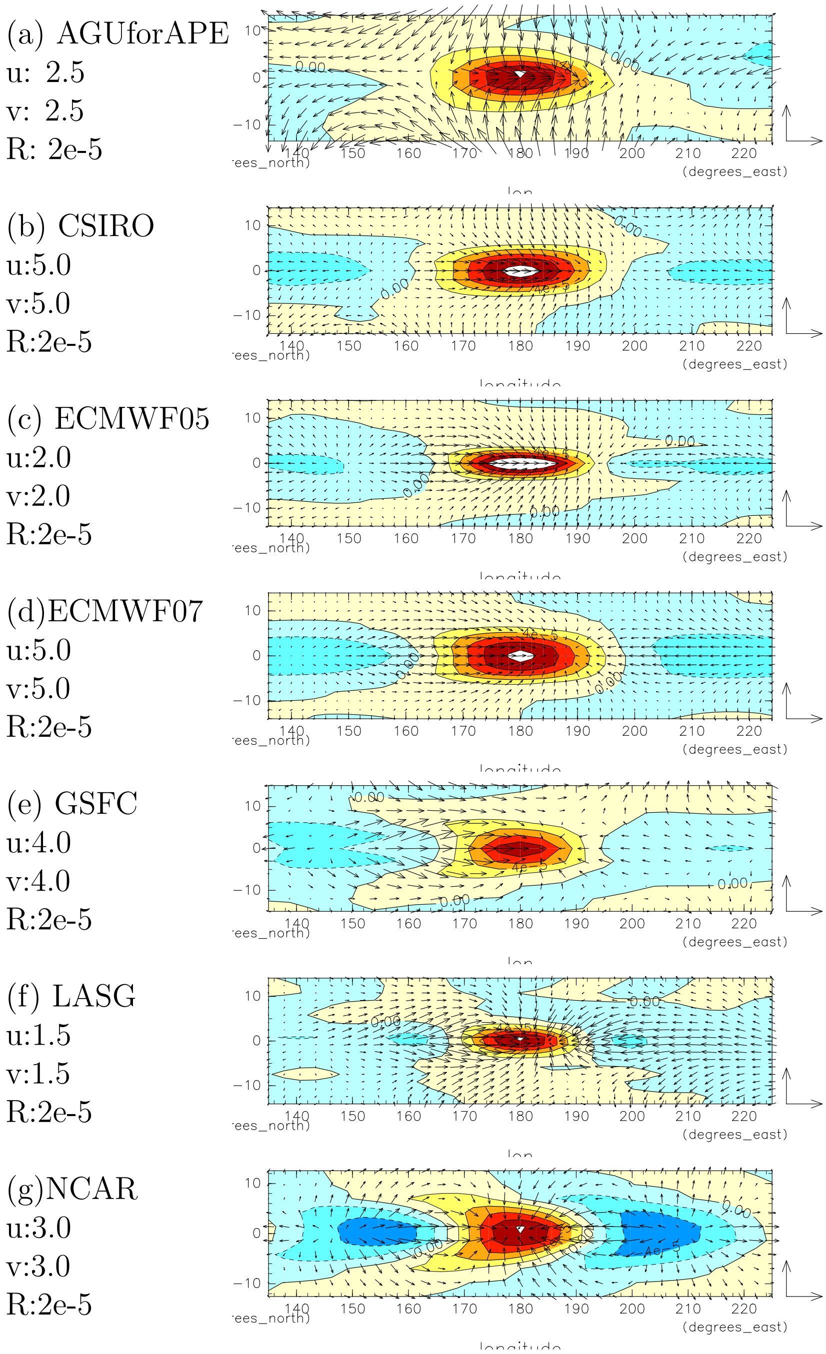

Fig. 8. Horizontal structures of composite anomalies of precipitation and wind vector at 925hPa for K component. Velocity scales for the unit vector and contour interval for precipitation are given to the left in [m/s] and [Kg/m^{2}s], respectively.

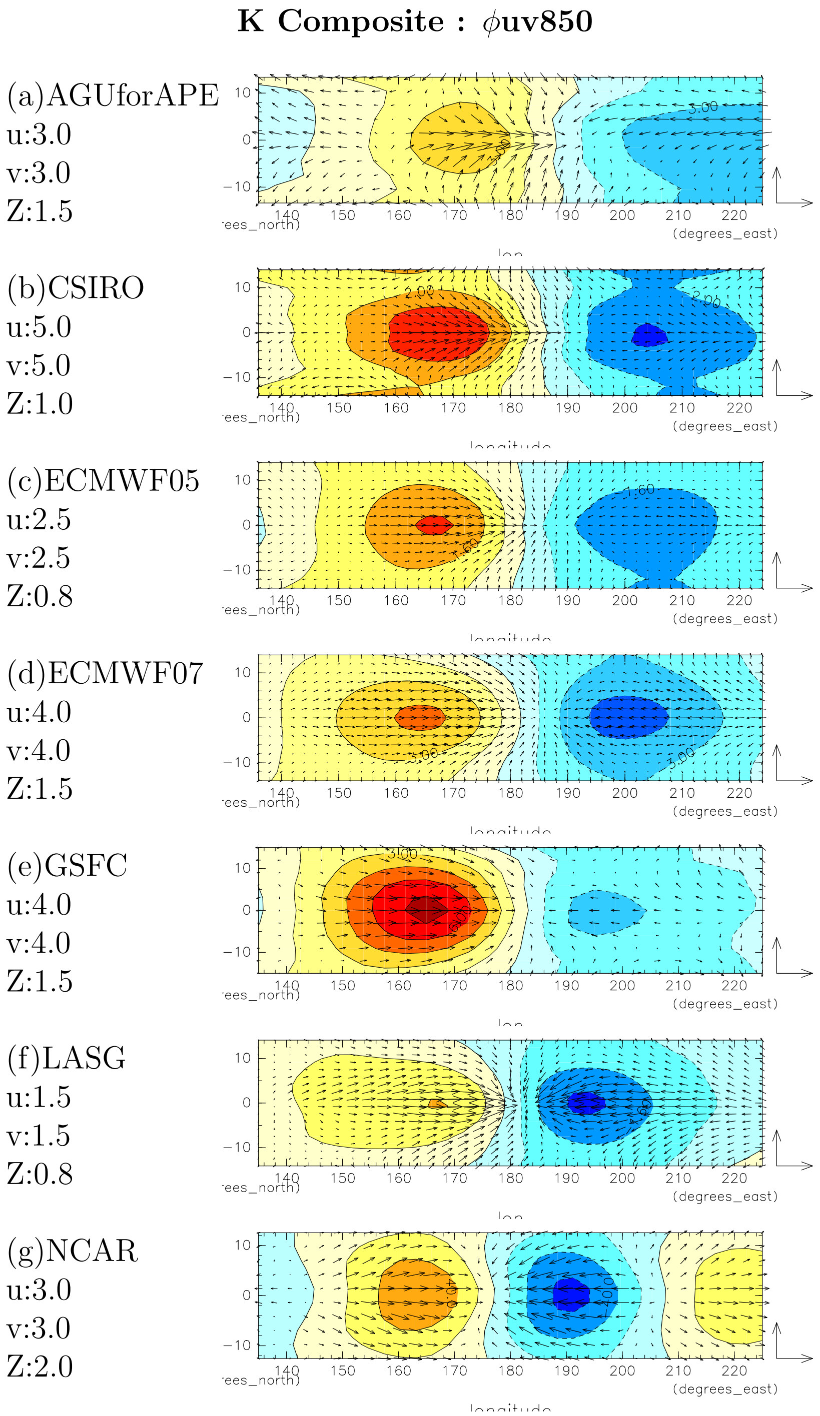

Fig. 9. Same as Fig.8 but for geopotential height and wind vector at 850hPa. Units for velocity scales and geopotential height are [m/s] and [m], respectively.

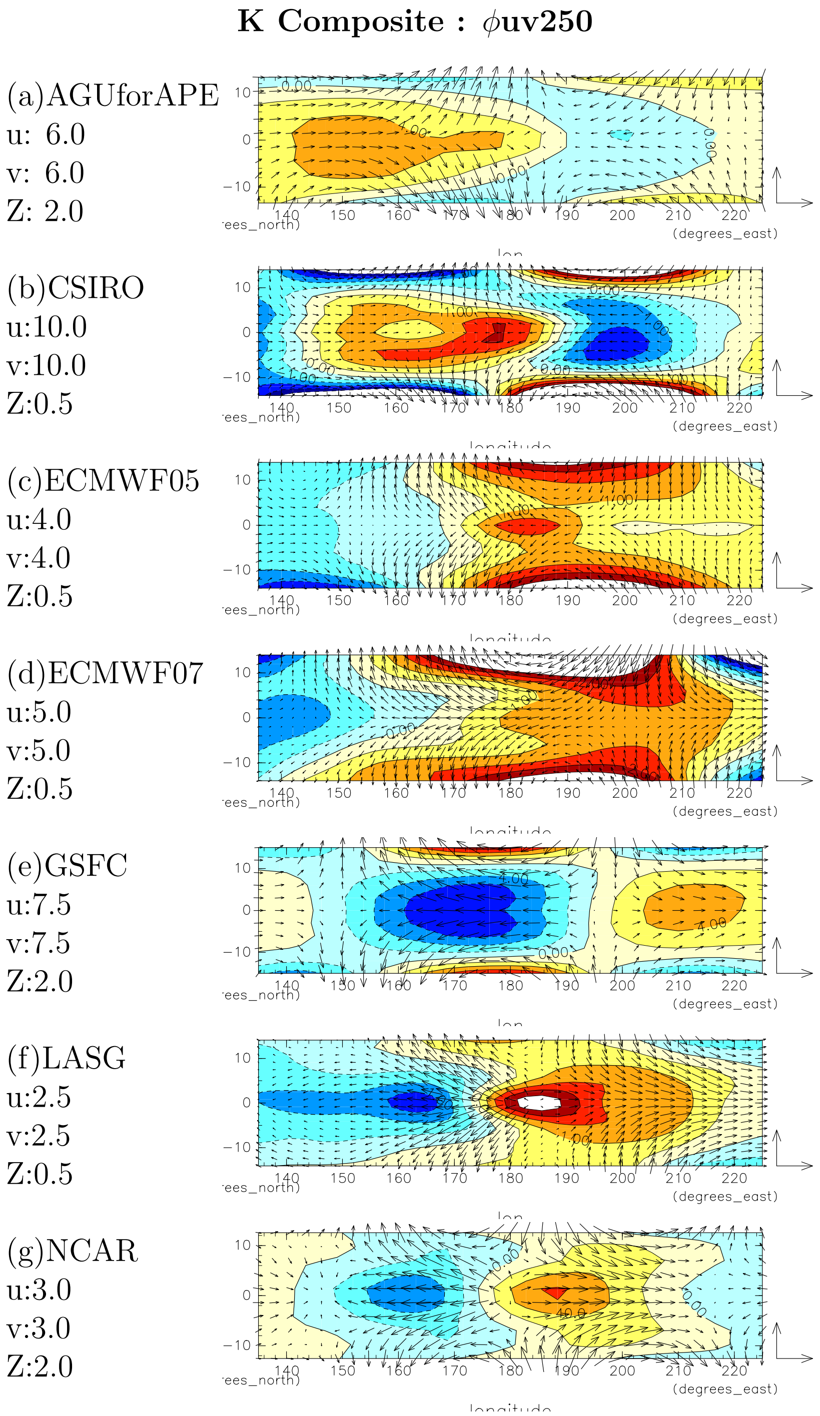

Fig. 10. Same as Fig.8 but for geopotential height and wind vector at 250hPa. Units for velocity scales and geopotential height are [m/s] and [m], respectively.

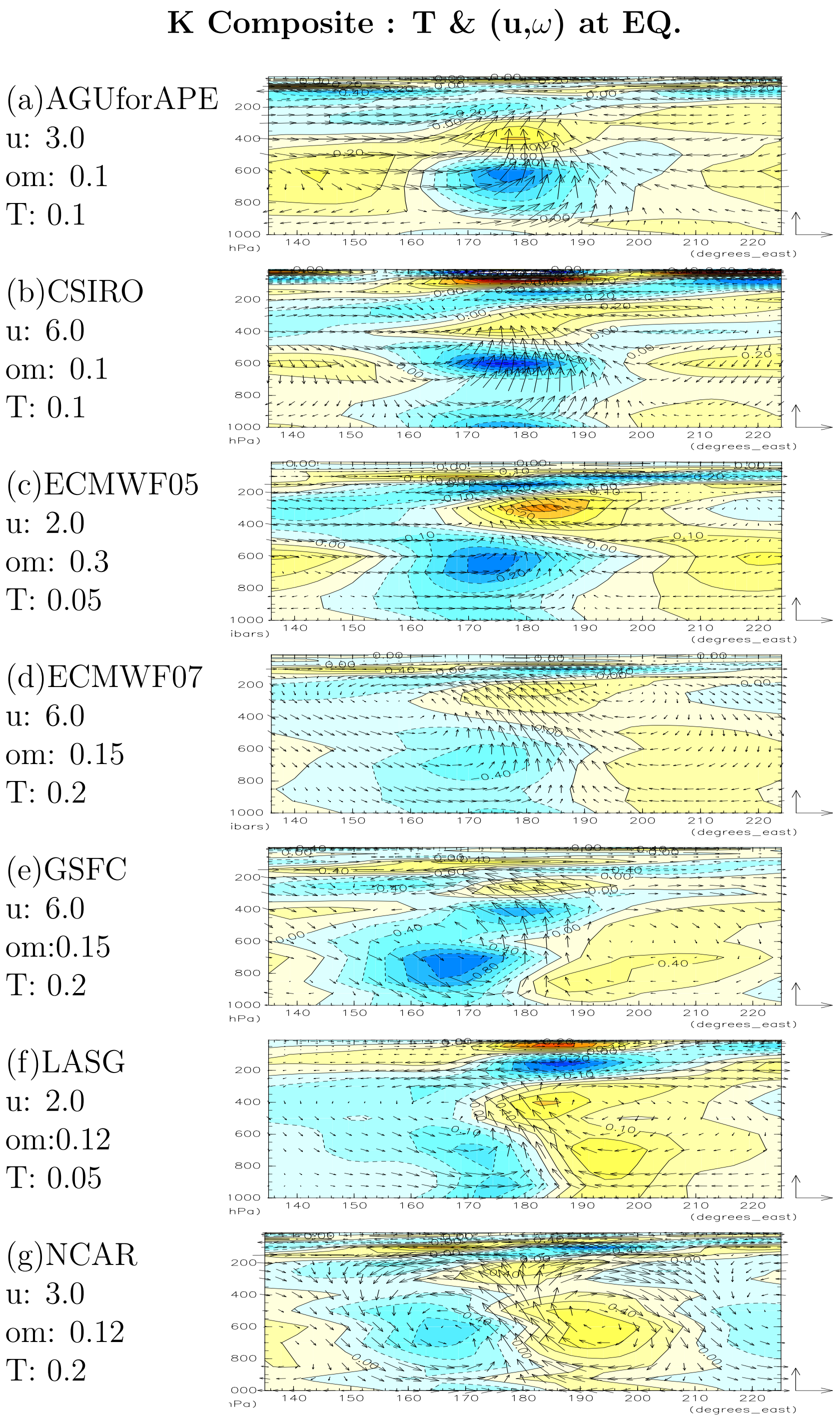

Fig. 11. Vertical structures of composite anomalies of temperature, zonal wind and p-vertical velocity along the equator for K component. Velocity scales for the unit vector and contour interval for temperature are given to the left in ([m/s],[Pa/s]) and [K], respectively.

K Composite : Q & (u,ω) at EQ.

(a)AGUforAPE
u: 3.0
om: 0.1
Q:1e-4

(b)CSIRO
u: 6.0
om: 0.1
Q:1e-4

(c)ECMWF05
u: 2.0
om: 0.3
T:5e-5

(d)ECMWF07
u: 6.0
om: 0.15
Q: 1e-4

(e)GSFC
u: 6.0
om:0.15
Q:1e-4

(f)LASG
u: 2.0
om:0.12
Q:5e-5

(g)NCAR
u: 3.0
om:0.12
Q:1e-4

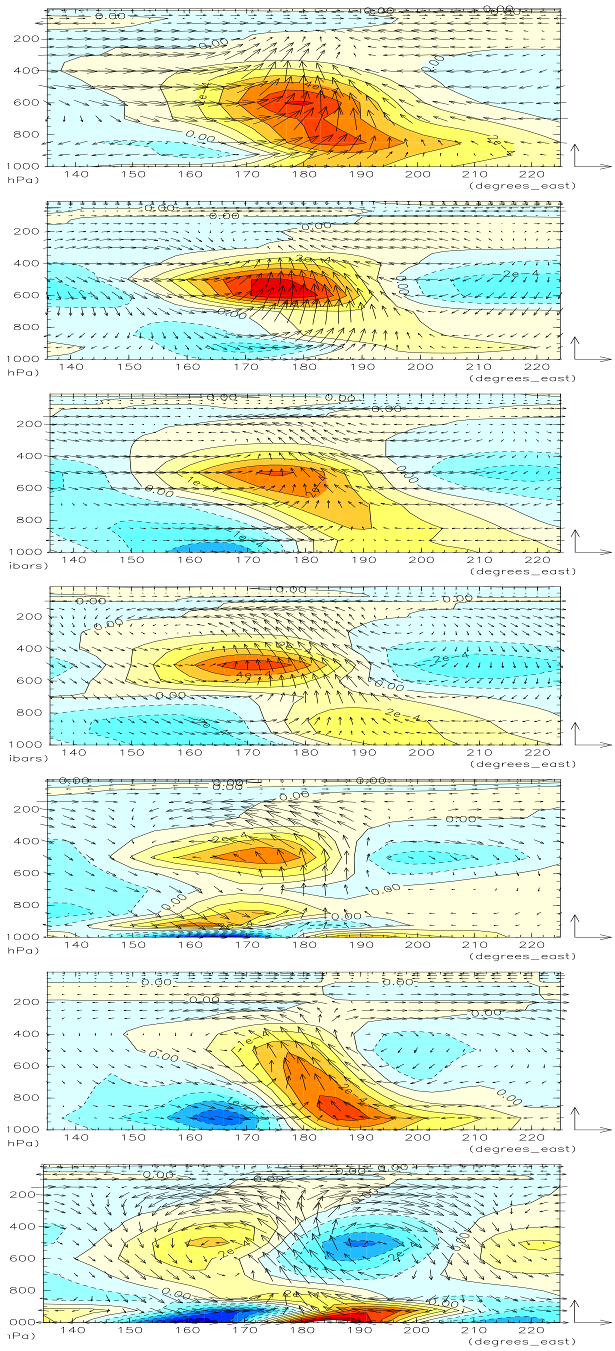

Fig. 12. Same as Fig.11 but for mixing ratio (unit is [kg/kg]).

K Composite : DT_CONV at EQ.

(a)AGUforAPE

$\dot{T}_{conv}$
2.5e-6

(b)CSIRO

data unavailable

(c)ECMWF05

$\dot{T}_{conv}$
4e-6

(d)ECMWF07

$\dot{T}_{conv}$
1.2e-5

(e)GSFC

$\dot{T}_{conv}$
8e-6

(f)LASG

$\dot{T}_{conv}$
5e-6

(g)NCAR

$\dot{T}_{conv}$
1e-5

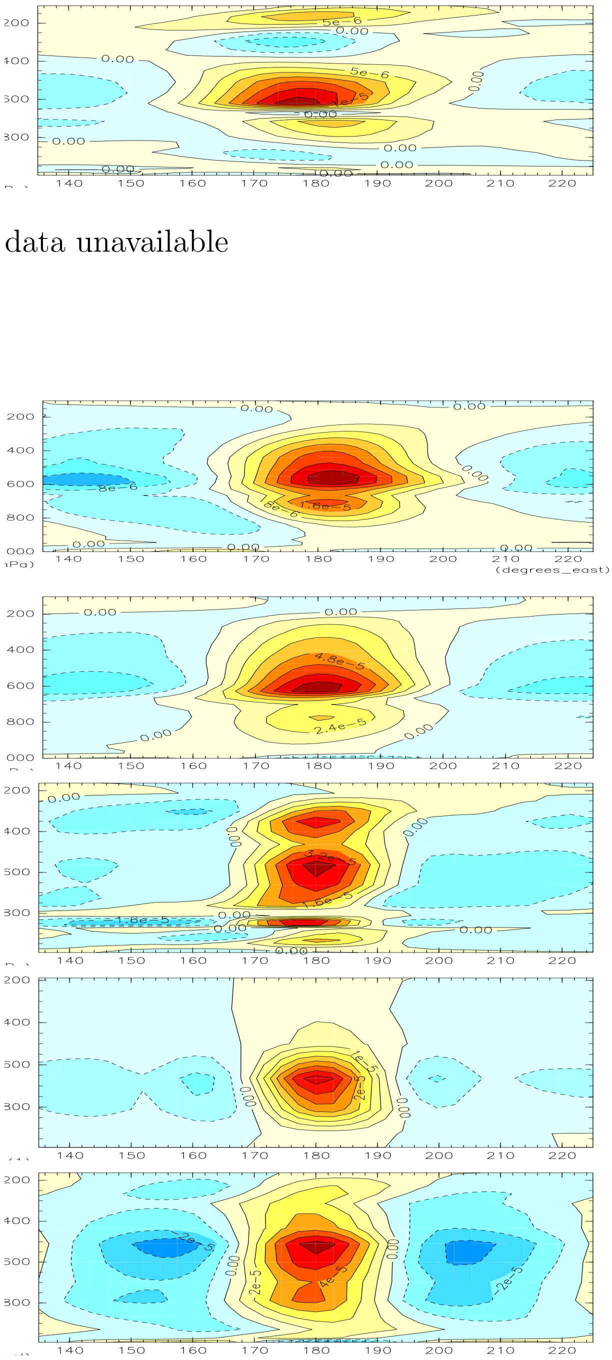

Fig. 13. Vertical structures of composite anomalies of parameterized convection heating along the equator for K component. Units is [K/s].

K Composite : DT_CLD at EQ.

(a)AGUforAPE

$\dot{T}_{cld}$
1.5e-5

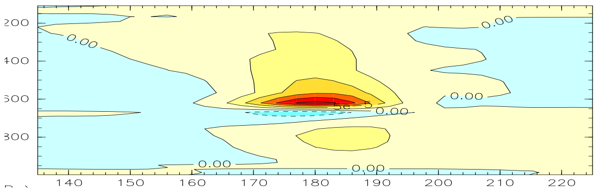

(b)CSIRO

data unavailable

(c)ECMWF05

$\dot{T}_{cld}$
5e-6

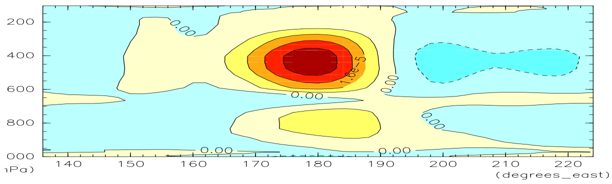

(d)ECMWF07

$\dot{T}_{cld}$
3e-6

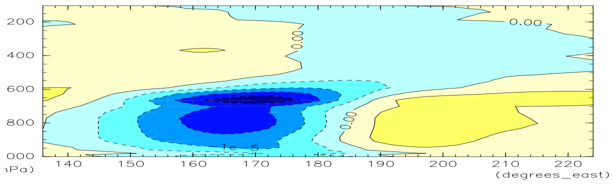

(e)GSFC

$\dot{T}_{cld}$
8e-6

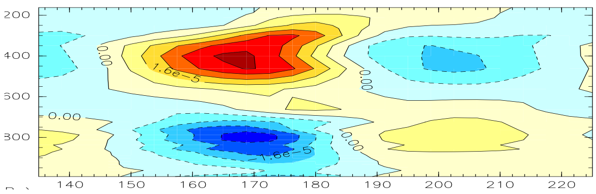

(f)LASG

data unavailable

(g)NCAR

$\dot{T}_{cld}$
2.5e-6

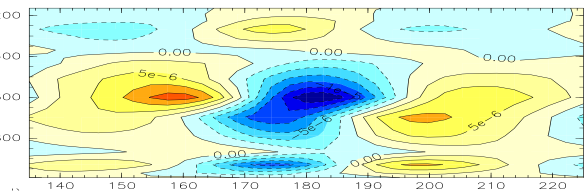

Fig. 14. Same as Fig.13 but for resolved cloud heating.

WIG Composite : RAIN & uv925

(a)AGUforAPE
u:1.0
v:1.0
R:2e-5

(b)CSIRO
u:1.5
v:1.5
R:2e-5

(c)ECMWF05
u:1.0
v:1.0
R:2e-5

(d)ECMWF07
u:1.5
v:1.5
R:2e-5

(e)GSFC
u:2.5
v:2.5
R:2e-5

(f)LASG
u:2.0
v:2.0
R:2e-5

(g)NCAR
u:1.5
v:1.5
R:2e-5

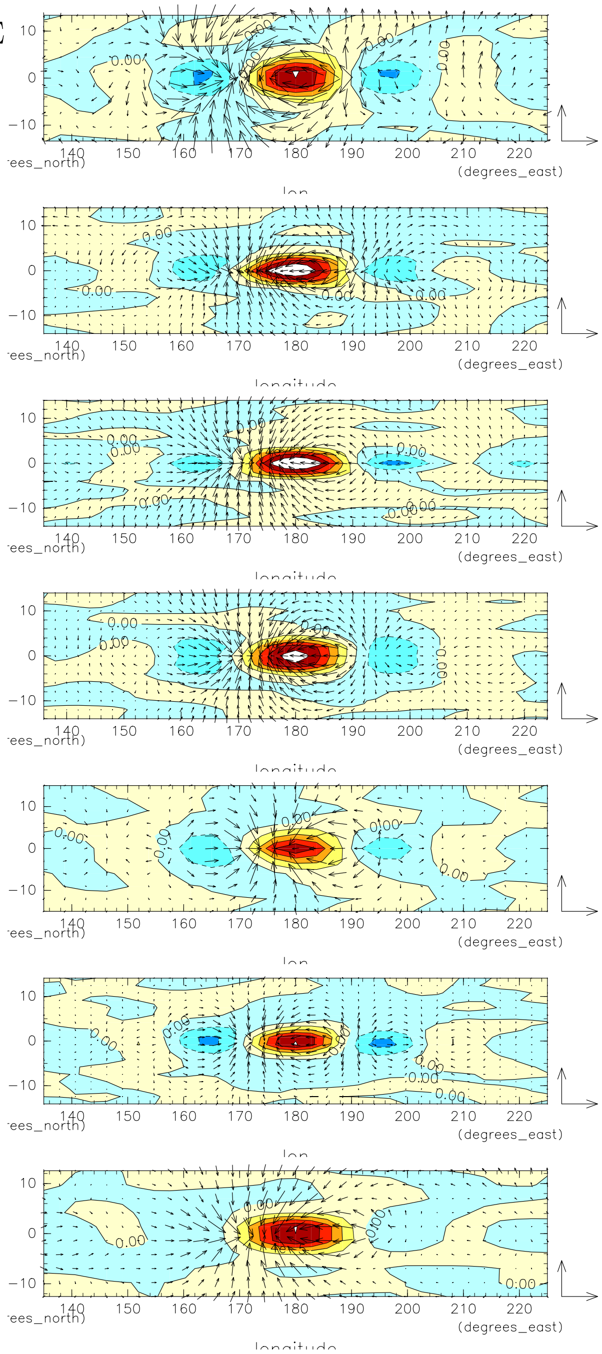

Fig. 15. Same as Fig.8 but for WIG component.

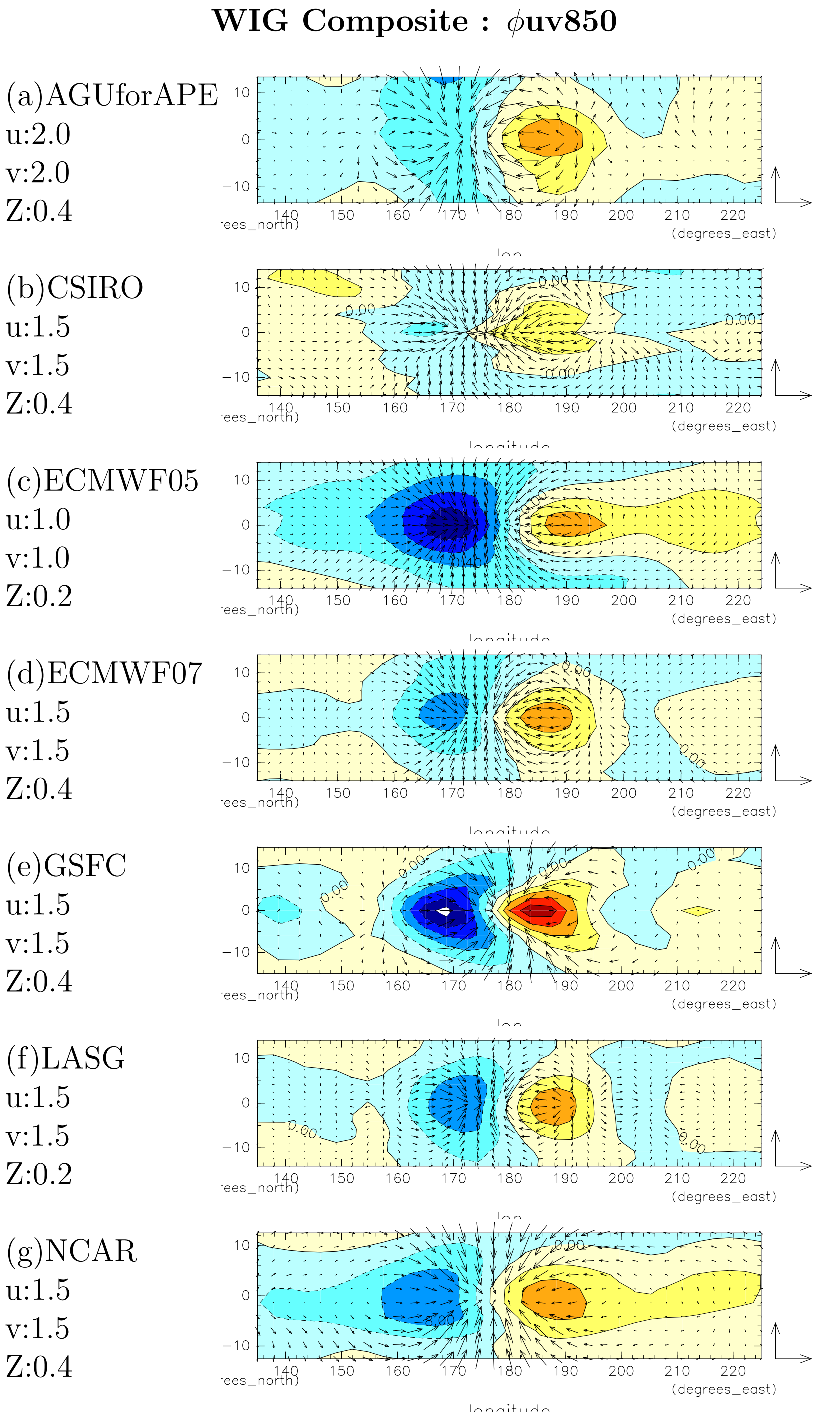

Fig. 16. Same as Fig.9 but for WIG component.

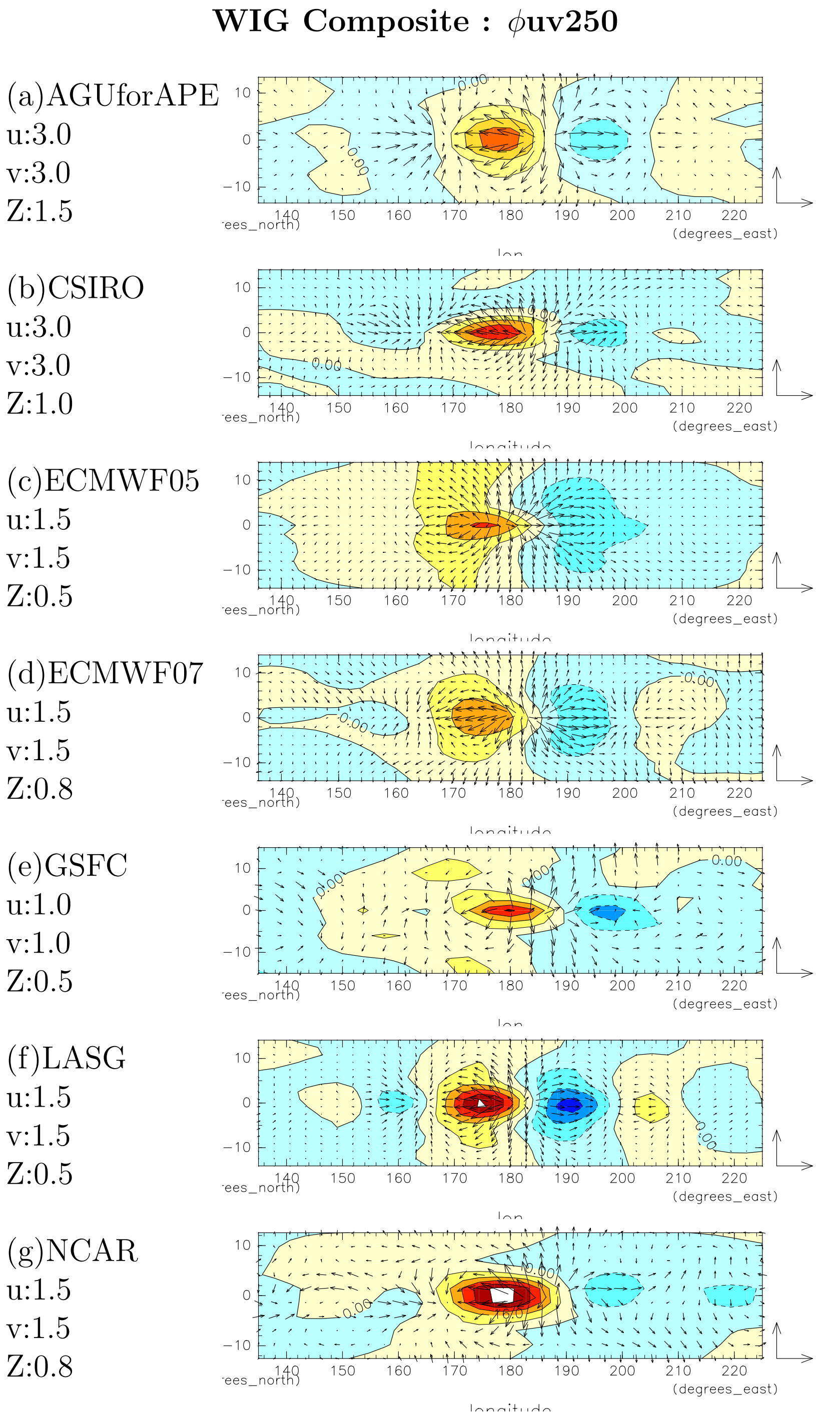

Fig. 17. Same as Fig.10 but for WIG component.

WIG Composite : T & (u,ω) at EQ.

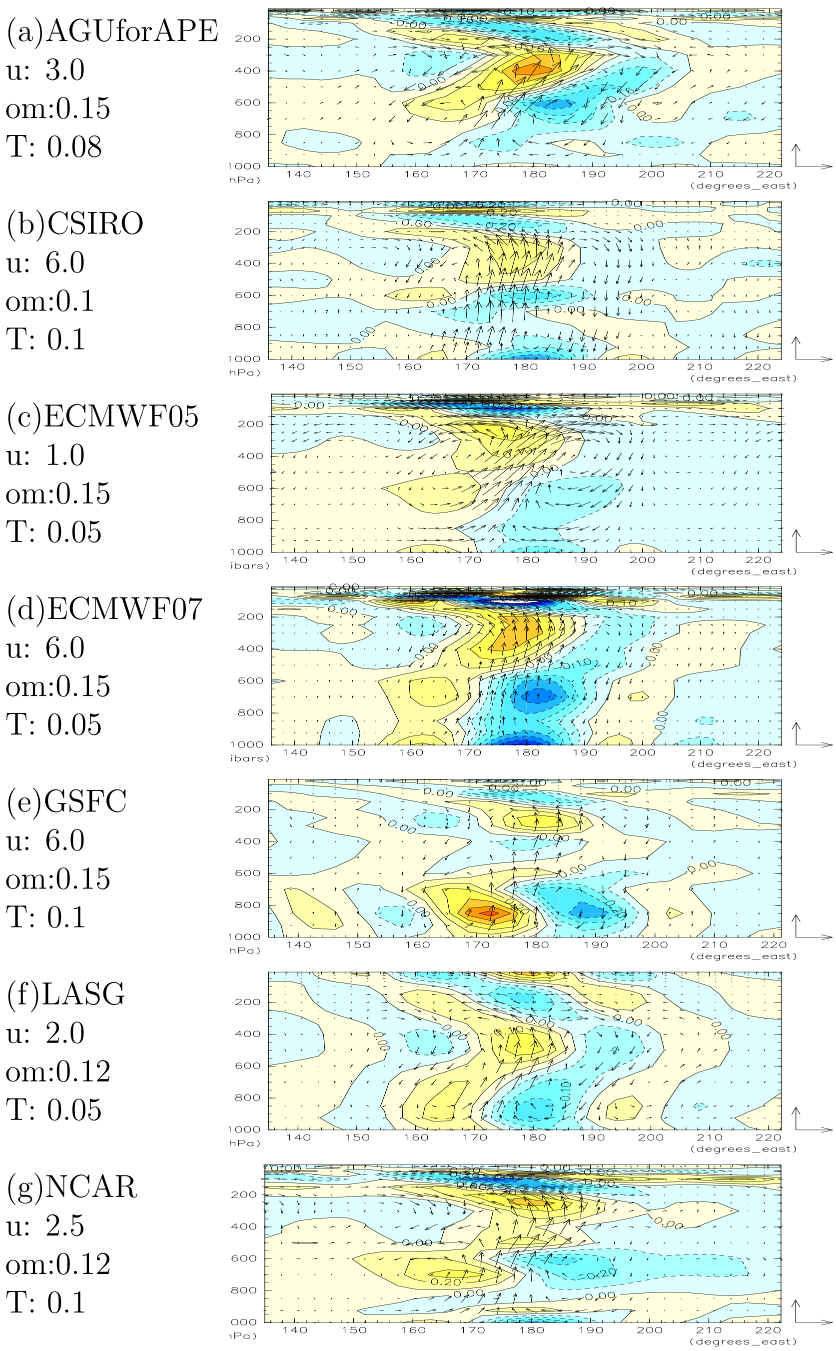

Fig. 18. Same as Fig.11 but for WIG component.

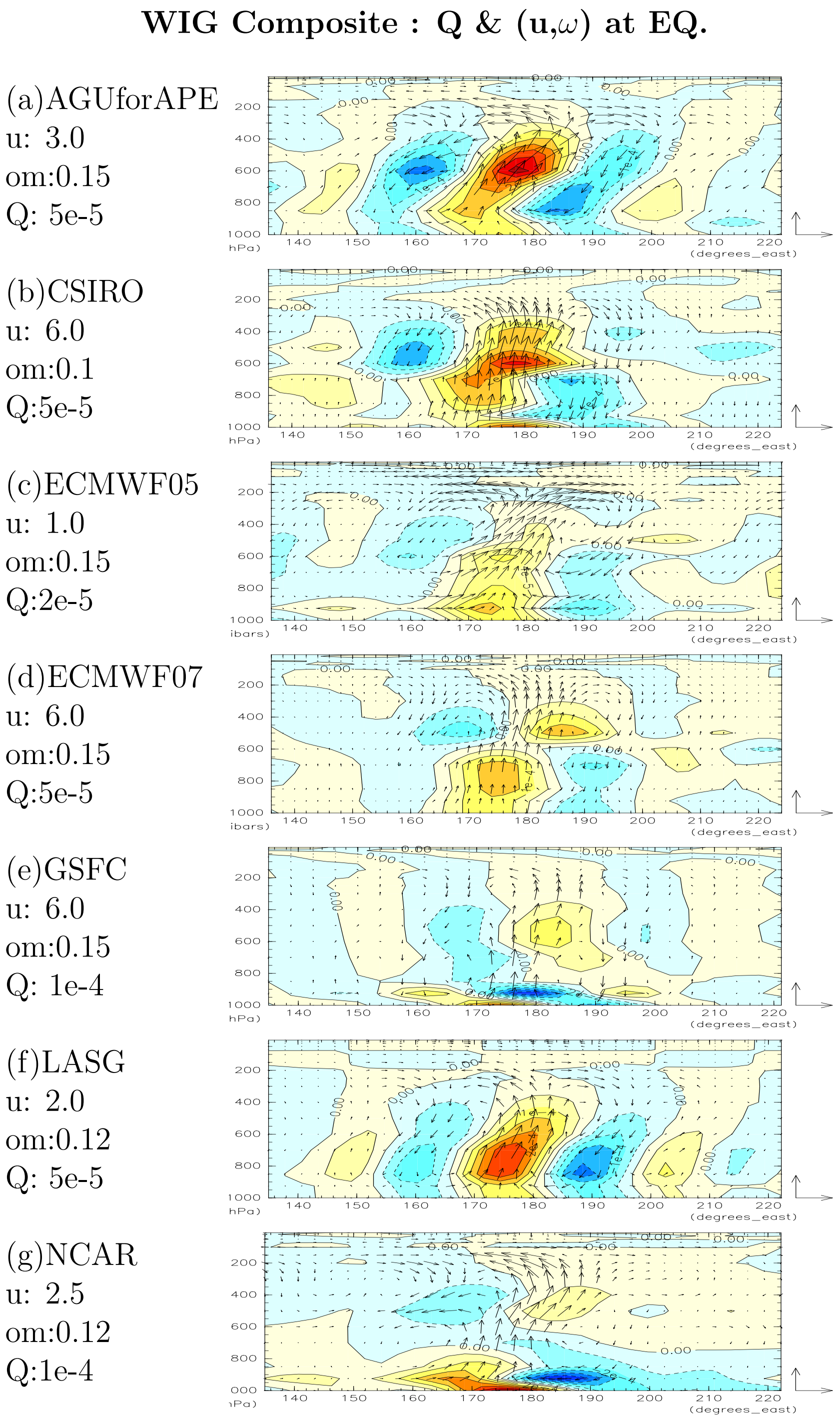

Fig. 19. Same as Fig.12 but for WIG component.

WIG Composite : DT_CONV at EQ.

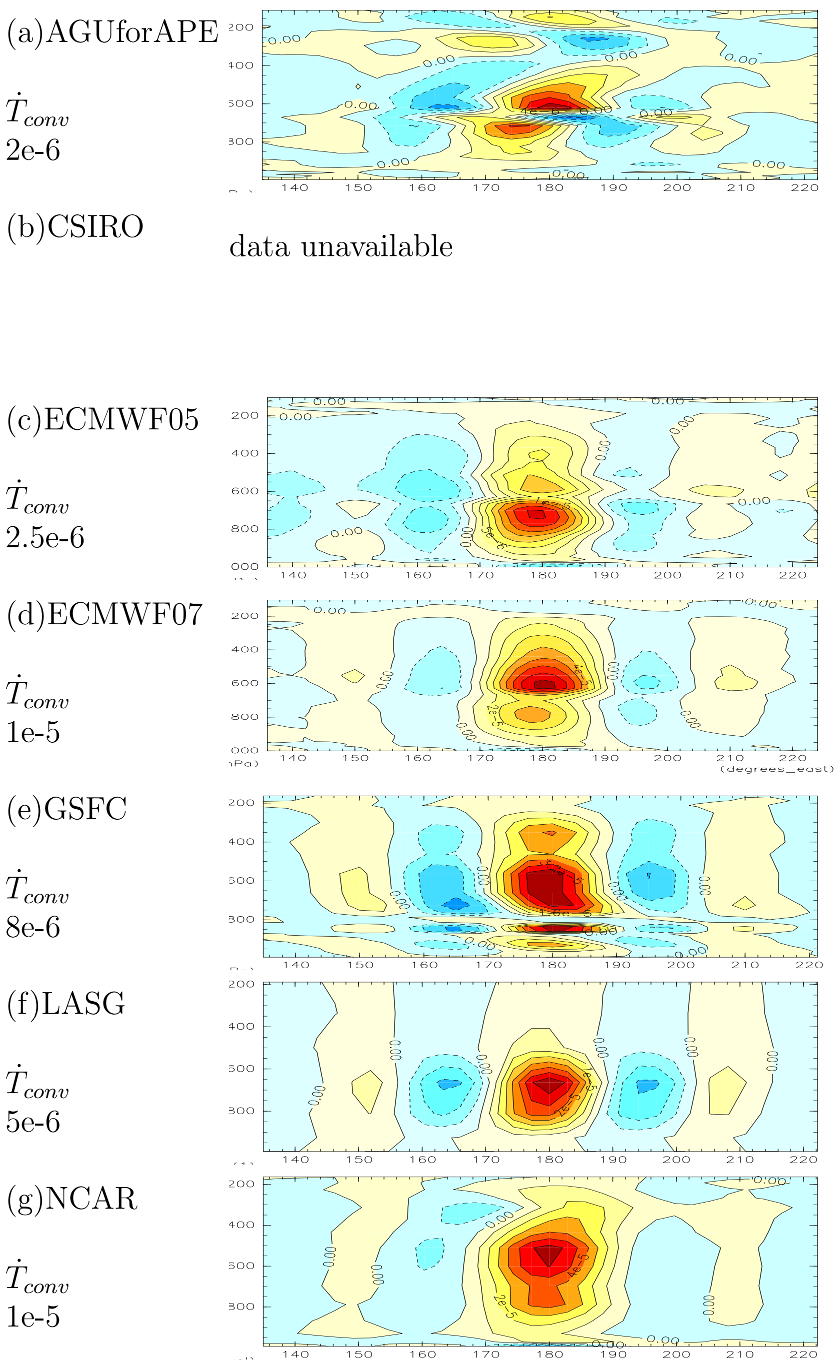

Fig. 20. Same as Fig.13 but for WIG component.

WIG Composite : DT_CLD at EQ.

(a)AGUforAPE

$\dot{T}_{cld}$
2e-5

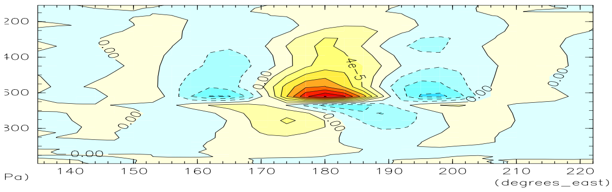

(b)CSIRO

data unavailable

(c)ECMWF05

$\dot{T}_{cld}$
5e-6

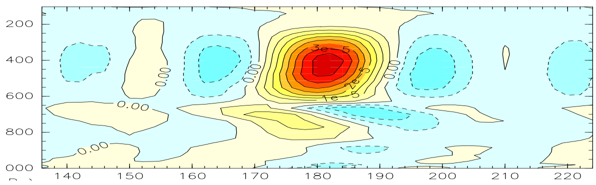

(d)ECMWF07

$\dot{T}_{cld}$
2.5e-6

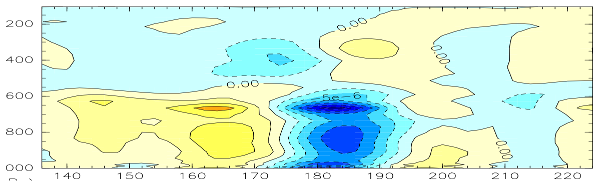

(e)GSFC

$\dot{T}_{cld}$
6e-6

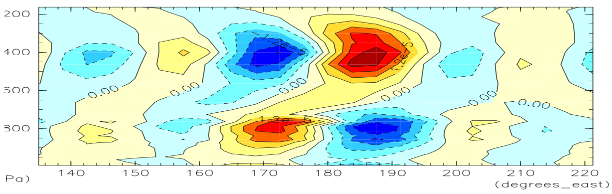

(f)LASG

data unavailable

(g)NCAR

$\dot{T}_{cld}$
2.5e-6

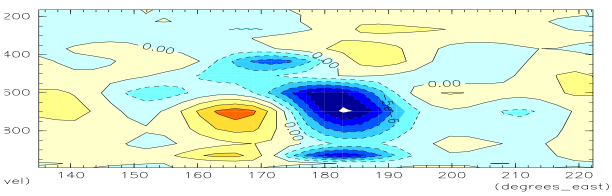

Fig. 21. Same as Fig.14 but for WIG component.

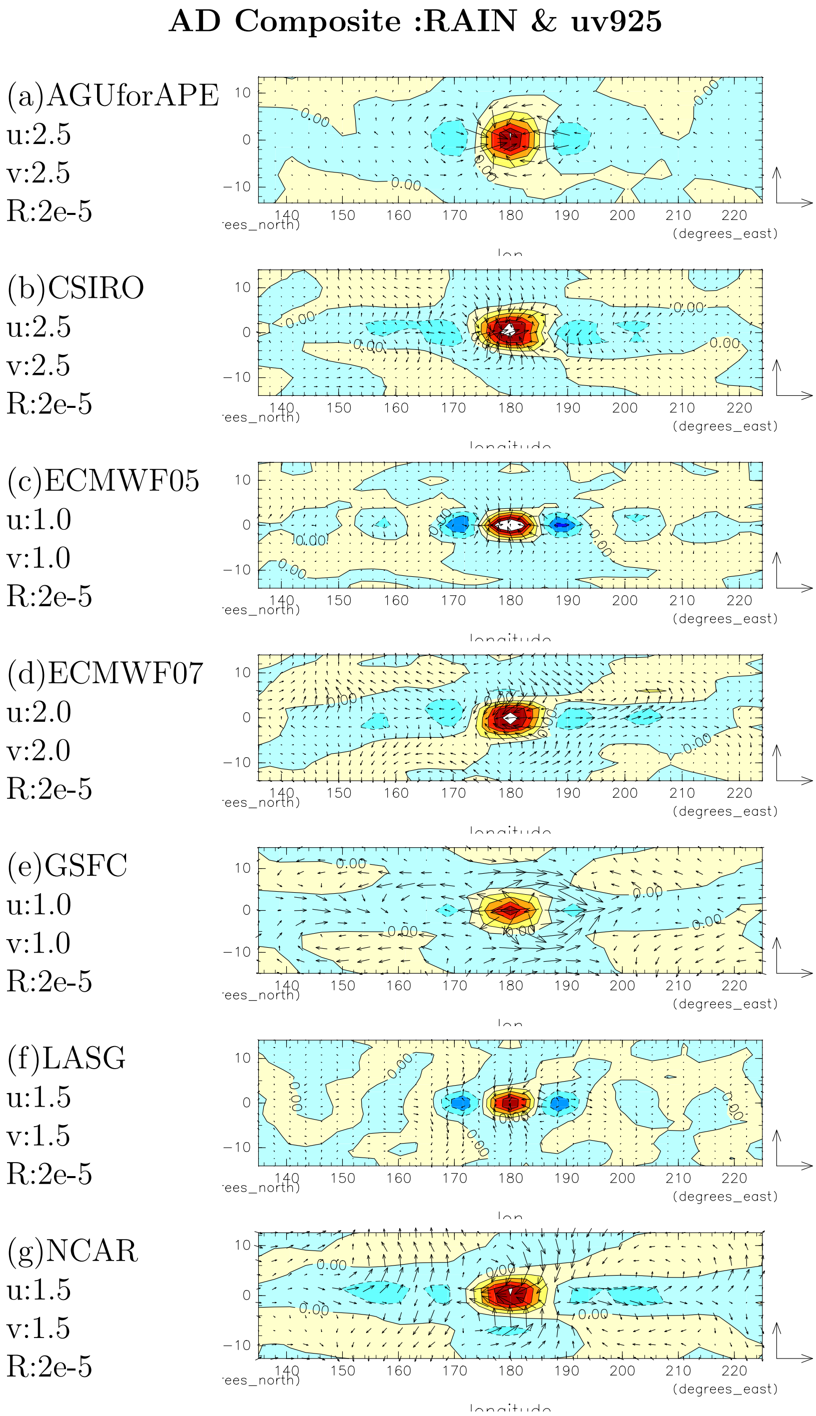

Fig. 22. Same as Fig.8 but for AD component.

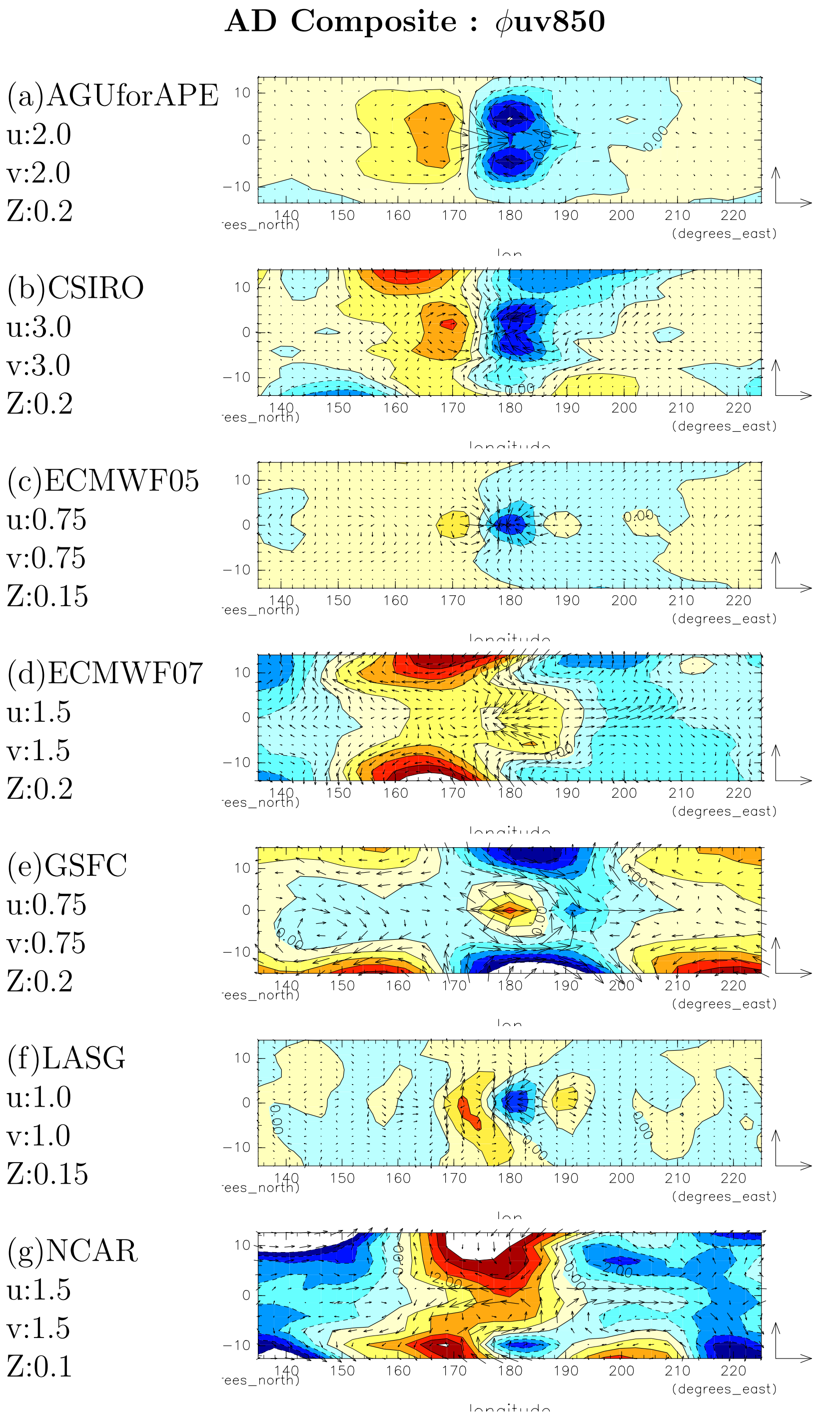

Fig. 23. Same as Fig.9 but for AD component.

AD Composite : ϕuv250

(a)AGUforAPE
u:1.5
v:1.5
Z:0.5

(b)CSIRO
u:2.0
v:2.0
Z:1.0

(c)ECMWF05
u:1.0
v:1.0
Z:0.2

(d)ECMWF07
u:2.5
v:2.5
Z:0.5

(e)GSFC
u:2.5
v:2.5
Z:1.0

(f)LASG
u:1.0
v:1.0
Z:0.5

(g)NCAR
u:3.0
v:3.0
Z:1.0

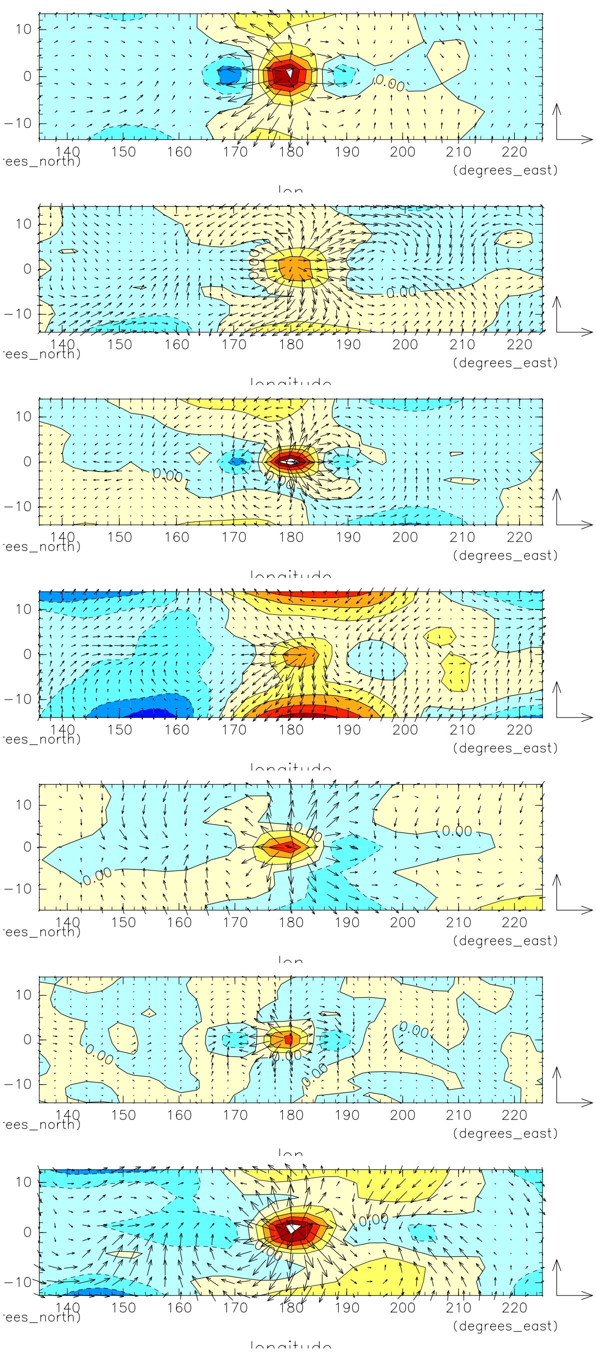

Fig. 24. Same as Fig.10 but for AD component.

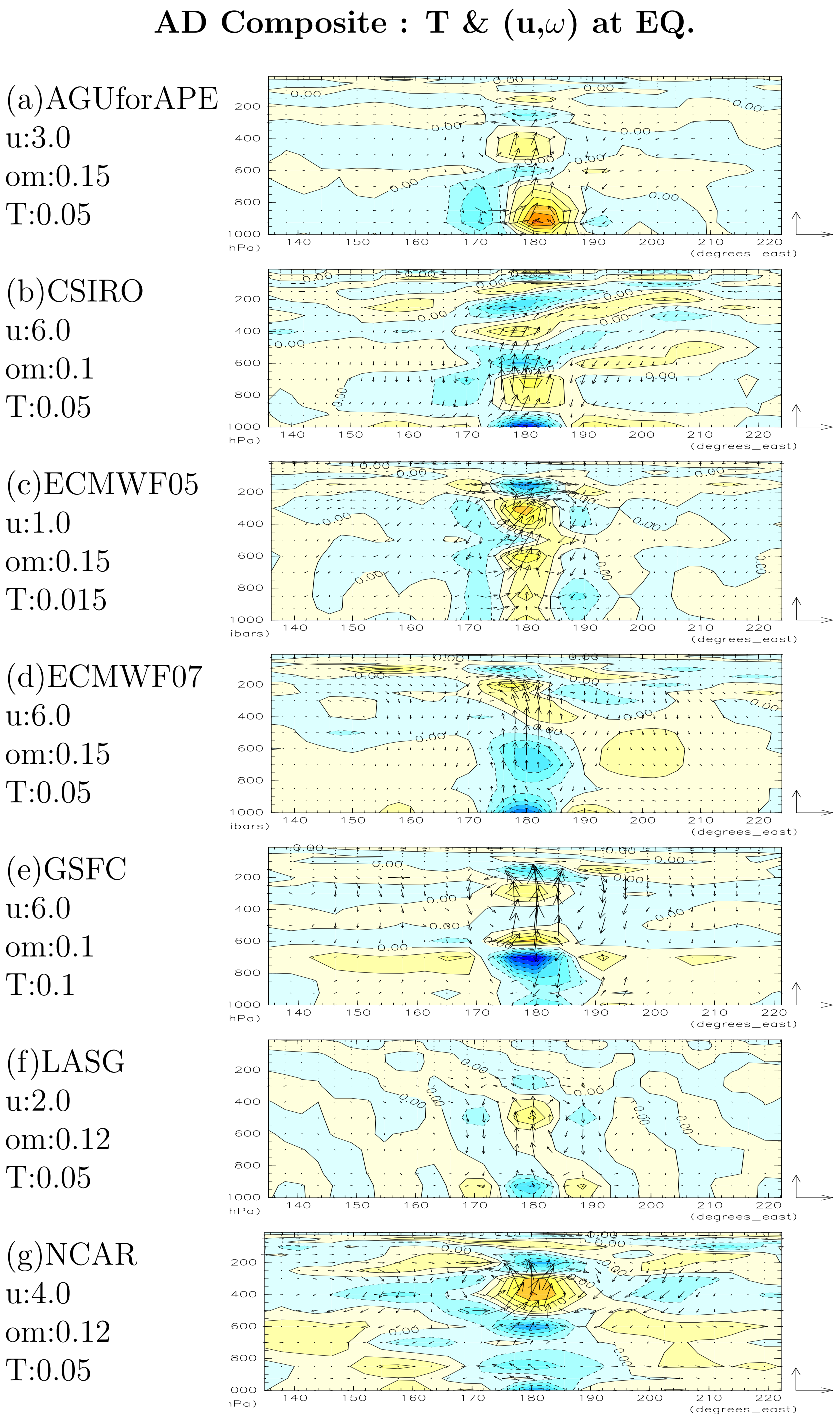

Fig. 25. Same as Fig.11 but for AD component.

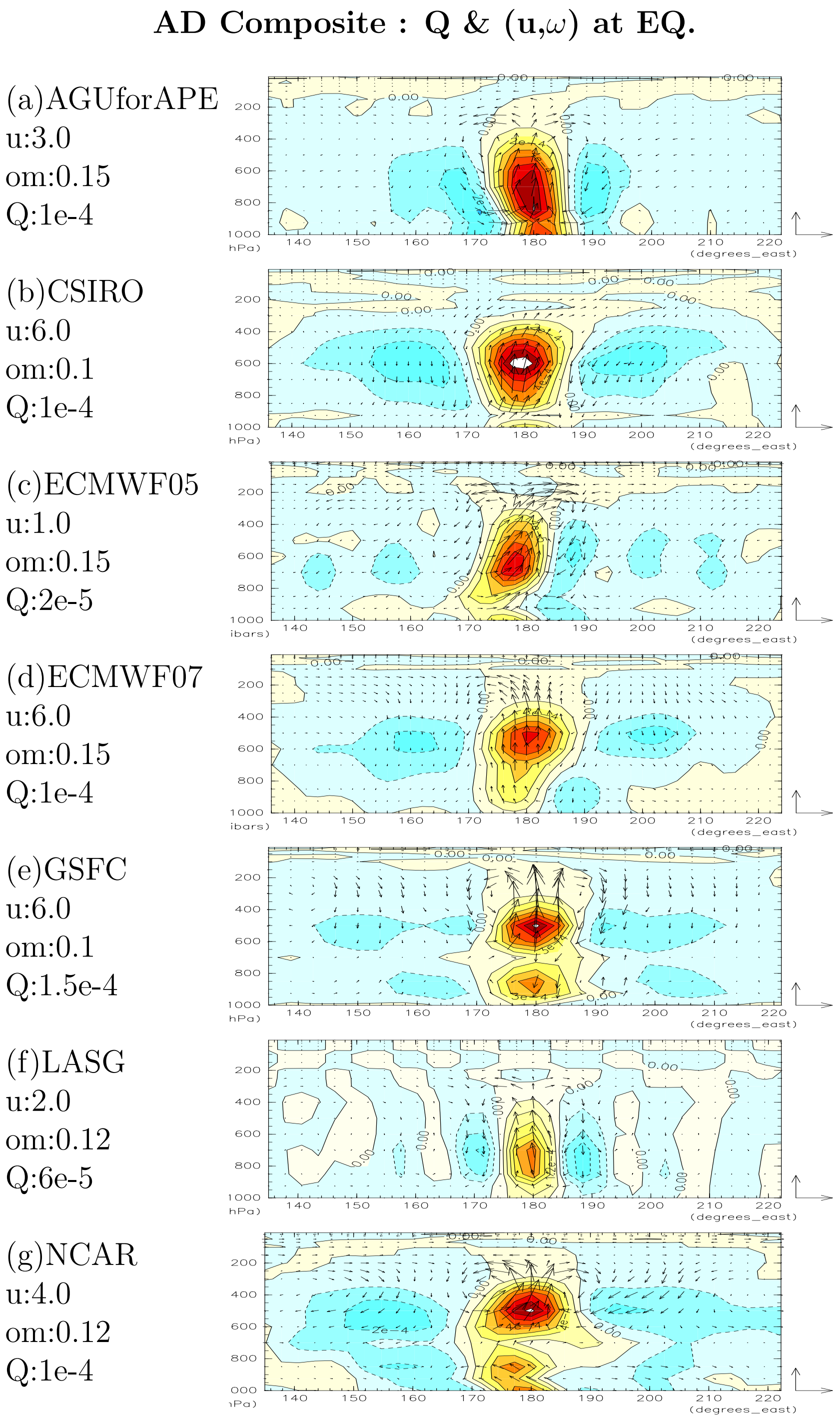

Fig. 26. Same as Fig.12 but for AD component.

AD Composite : DT_CONV at EQ.

(a)AGUforAPE

$\dot{T}_{conv}$
2e-6

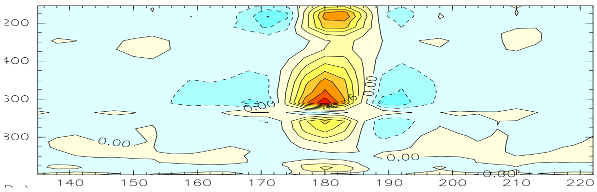

(b)CSIRO

data unavailable

(c)ECMWF05

$\dot{T}_{conv}$
2e-6

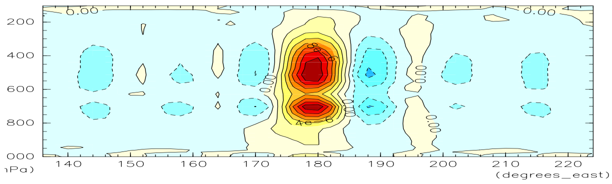

(d)ECMWF07

$\dot{T}_{conv}$
1e-5

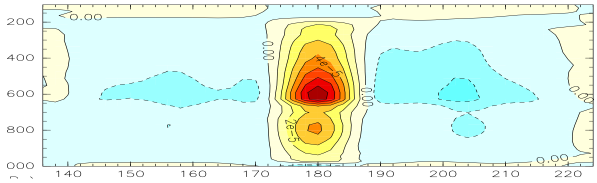

(e)GSFC

$\dot{T}_{conv}$
5e-6

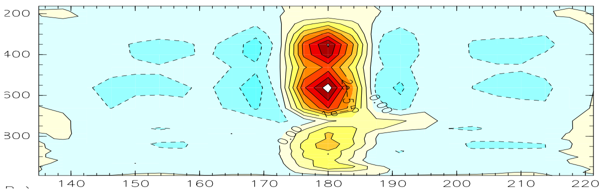

(f)LASG

$\dot{T}_{conv}$
1e-5

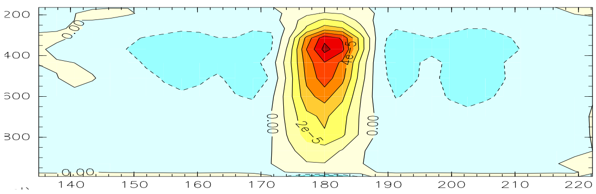

(g)NCAR

$\dot{T}_{conv}$
6e-6

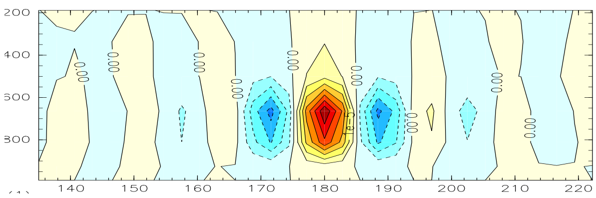

Fig. 27. Same as Fig.13 but for AD component.

AD Composite : DT_CLD at EQ.

(a)AGUforAPE

$\dot{T}_{cld}$
1.5e-5

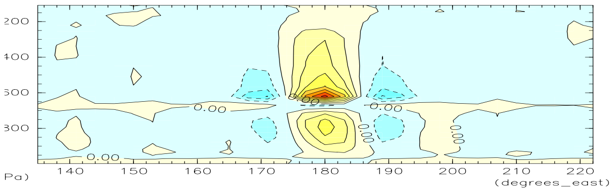

(b)CSIRO

data unavailable

(c)ECMWF05

$\dot{T}_{cld}$
5e-6

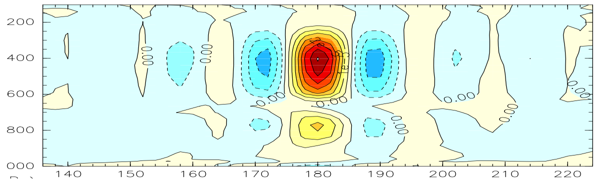

(d)ECMWF07

$\dot{T}_{cld}$
3e-6

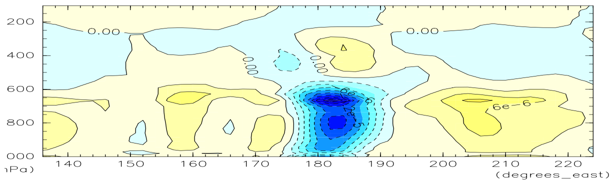

(e)GSFC

$\dot{T}_{cld}$
1.2e-5

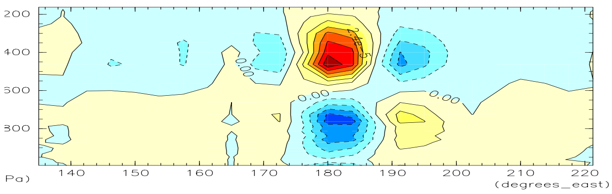

(f)LASC

data unavailable

(g)NCAR

$\dot{T}_{cld}$
3e-6

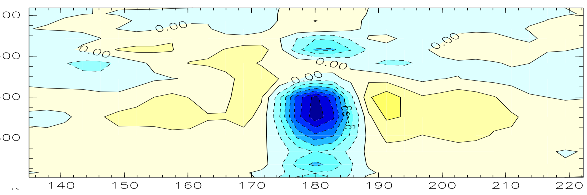

Fig. 28. Same as Fig.14 but for AD component.

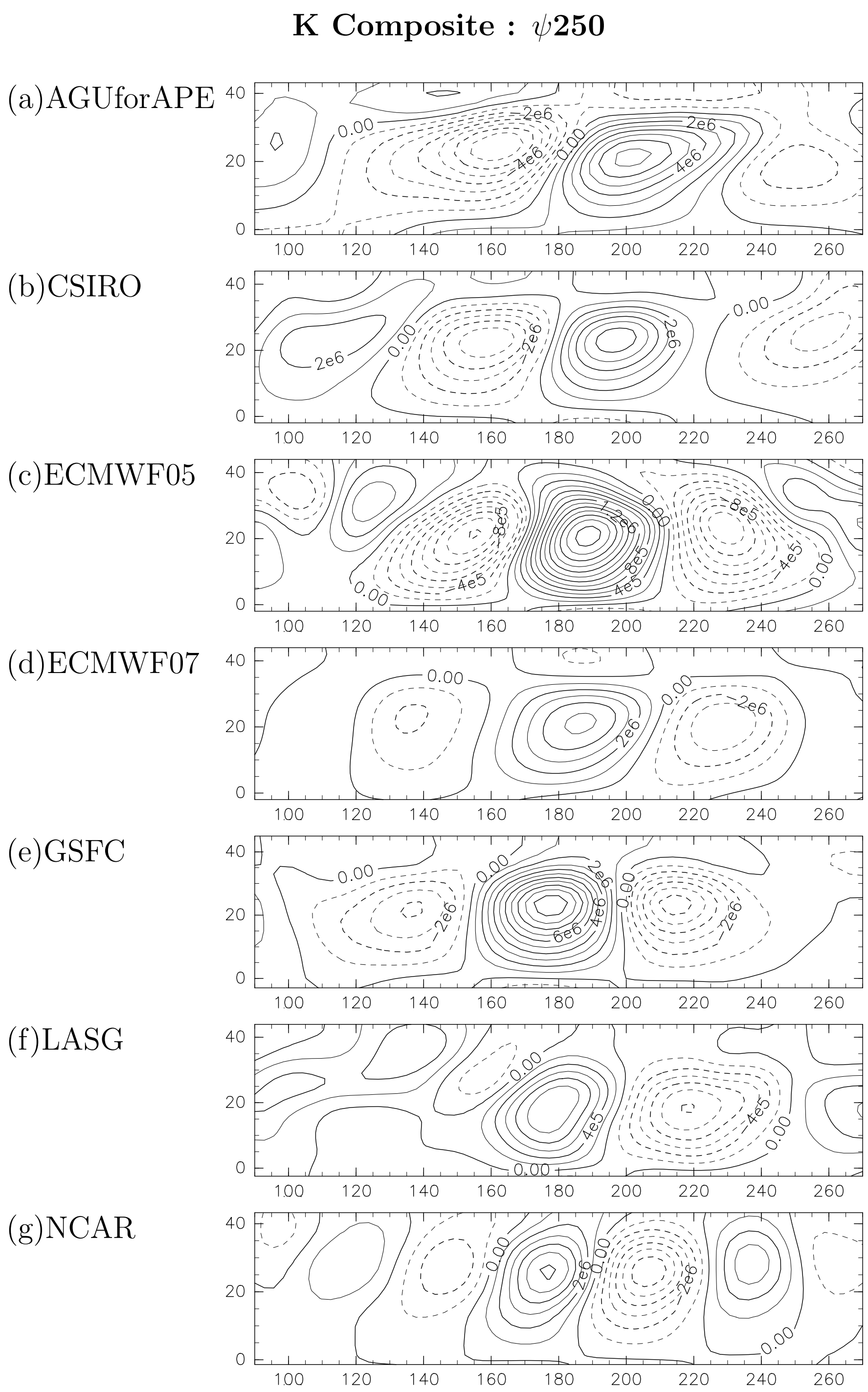

Fig. 29. Horizontal structures of composite anomalies of stream function at 250hPa. for K component. Contour interval is 2×10^{-5} [m] for ECMWF05 and LASG, and is 10^{-6} [m] for the other models.

List of Tables

Table 1. Participating models

GROUP SYMBOL	MODEL	HORIZONTAL RESOLUTION	NO.OF LEVELS	DEEP CONVECTION	COM-POSITE
AGUforAPE	AFES	T39	48	Emanuel	yes
CGAM	HadAM3	3.75° x 2.5°	30	Gregory-Rawntree	-
CSIROstd	CCAM-05e	∼210km	18	McGregor	yes
CSIROold	CCAM-05a	∼210km	18	McGregor	-
DWD	GME	∼1°	31	Tiedtke	-
ECMWF05	IFS cy29r2	T159	60	Bechtold *et al.* 2004	yes
ECMWF07	IFS cy32r3	T159	60	Bechtold *et al.* 2008	yes
FRCGC	NICAM	∼7km	54	None	-
GFDL	AM2.1	2.5° x 2°	24	RAS	-
GSFC	NSIPP-1	3.75° x 3°	34	RAS	yes
K1JAPAN	CCSR/NIES 5.7	T42	20	Pan-Randall	-
LASG	SAMIL	R42	9	Manabe	yes
MIT	MIT-GCM	∼280km	40	RAS	-
MRI	MRI/JMA98	T42	30	Randall-Pan	-
NCAR	CCSM-CAM3	T42	26	Zhang-McFarlane	yes
UKMOn48	pre-HadGAM1	3.75° x 2.5°	38	Gregory 1999	-
UKMOn96	pre-HadGAM1	1.875° x 1.25°	38	Gregory 1999	-